Amyloid beta glycation leads to 1 neuronal mitochondrial dysfunction and Alzheimer's pathogenesis through VDAC1-dependent mtDNA efflux

Firoz Akhter[1, *], Asma Akhter[1, *], Hillary Schiff[2], Arianna Maffei[2,6], Xiongwei Zhu[3], Justin Douglas[4], Zhen Zhao[5], Donghui Zhu[1,6, #]

[1]Department of Biomedical Engineering, Stony Brook University, Stony Brook, NY 11794, United States
[2]Department of Neurobiology and Behavior, Stony Brook University, Stony Brook, NY 11794, United States.
[3]Department of Pathology, Case Western Reserve University, Cleveland, OH 44106, United Sates
[4]Nuclear Magnetic Resonance Core Lab, University of Kansas, Lawrence, Kansas 66045, United State
[5]Department of Physiology and Neuroscience, Zilkha Neurogenetic Institute, Keck School of Medicine, University of Southern California, Los Angeles, CA 90033, United States
[6]Neuroscience Graduate Program, Renaissance School of Medicine, Stony Brook University, Stony Brook, NY 11794, United States

[*]These authors contributed equally

[#]Corresponding author:

Donghui Zhu (donghui.zhu@stonybrook.edu)

Abstract
Amyloid beta (Aβ), a stable protein, undergoes posttranslational glycation, forming glycated Aβ (gAβ), an advanced glycation end product (AGE) observed in Alzheimer's disease (AD), yet the pathological role of gAβ remains understudied. This work explores gAβ's role in inducing neuronal mitochondrial DNA (mtDNA) efflux in a VDAC1-dependent manner and in activating the innate immune cGAS-STING pathway in AD. Findings demonstrate cGAS-mtDNA binding induced by gAβ in neuro-cytoplasm, along with cGAS-STING activation in aged AD mice and human AD brains. Knockdown of RAGE, cGAS, or STING protects APP mice from mitochondrial dysfunction and AD-like pathology, as does inhibiting VDAC1. Moreover, RAGE inhibition in APP knock-in mice, coupled with spatially enhanced resolution omics-sequencing, confirms downregulation of innate immune responses and disease-associated genes in AD. Therefore, this study identifies a crucial link between gAβ and innate immunity, indicating therapeutic targeting of VDAC1, RAGE, or cGAS-STING may enhance resilience against gAβ-related pathological insults in AD.

Main
Post-translational protein glycation is a non-enzymatic process in which sugars react with proteins, forming molecules known as advanced glycation end-products (AGEs), and it has long-been considered a toxic consequence of carbohydrate metabolism[1]. This process is implicated in various diseases, including neurodegenerative disorders like Alzheimer's disease (AD)[2]. Both amyloid beta (Aβ) and tau proteins are subject to glycation. Glycated tau in AD induces neuronal oxidative stress and neurodegeneration[3], while the effect of Aβ glycation is underexplored. An early study reported that Aβ is glycated with an age-dependent elevation of AGEs in Tg2576 mice, and gAβ is more toxic than native Aβ form[4], however the detailed molecular mechanisms of its deleterious effect are unclear.

Mounting evidence shows Aβ is highly glycated in patients, and senile plaques in AD brains are enriched with AGEs and have nearly three times more AGE adducts than age-matched controls, pointing to a potential involvement for this irreversible non-enzymatic post-translational alteration in AD, implying that Aβ is glycated[5-8]. Long-lived proteins are favored for AGE production, and Aβ's stability makes it a suitable substrate for glycation and Aβ-AGE (gAβ) formation[9]. Direct covalent crosslinking of gAβ to substrates or its binding to surface receptors, such as receptor for AGE (RAGE), leads to neuroinflammation and synaptic toxicity. gAβ with the altered secondary structure is a more suitable ligand than authentic Aβ for RAGE, resulting in the subsequent activation of signaling pathways that can lead to AD-like pathology. RAGE is a known multiligand receptor that can amplify innate immune and inflammatory responses as a progression factor[10]. Thus, we speculate that gAβ is more prone to bind to/activate RAGE and the downstream innate immune pathways that contribute to AD pathogenesis.

The cyclic GMP-AMP synthase (cGAS) - stimulator of interferon genes (STING) pathway acts as a critical mechanism for sensing of dsDNA in cytoplasm to trigger innate immune response[11,12]. Damage-associated molecular patterns (DAMP) such as mitochondrial DNA (mtDNA) can cause and maintain inflammation in various inflammatory or degenerative diseases including AD[13], upon entering the cytoplasm, extracellular space or circulation. cGAS, a cytosolic DNA sensor, will be activated when mtDNA escapes into the cytosol because of mitochondrial stress[14]. The cytosolic mtDNA can subsequently activate the noncanonical inflammasome, culminating in the activation of TANK-binding kinase 1 (TBK1) and the phosphorylation of the transcription factor interferon regulatory factor 3 (IRF3), both are involved in cellular inflammation and destruction[15]. In the brain STING is expressed highest in microglia, but it can also be detected abundantly in neurons[16]. However, it remains unclear if and how the cGAS-STING pathway is activated in neurons in AD.

As the most prevalent protein in mitochondrial outer membrane, voltage-dependent anion channel (VDAC) controls cell death, Ca^{2+} influx, metabolism, inflammasome activation, and other processes[17,18]. It has been reported that VDAC oligomer pores allow stressed mitochondria to release mtDNA[19]. The apoptosome complex, which includes cytoplasmic cytochrome c, sequentially activates caspase-9, as well as the apoptotic effector caspase-3 and caspase-7[20]. Together, these proteases effectively break a wide range of cell substrates to hasten the cell's demise. Despite this finding and those in the earlier reports, the notion that VDAC1 might directly mediate mtDNA efflux remains largely unclear.

This research explores gAβ's involvement in inducing neuronal mtDNA efflux dependent of VDAC1 and activating the cytosolic cGAS-STING sensing pathway as well as the subsequent AD pathogenesis.

Results

Aβ glycation in human AD brain is linked to mtDNA leakage and cGAS-STING activation

Aβ are increasingly shown to be highly glycated in patients[21,22], pointing to a potential involvement for this irreversible, non-enzymatic post-translational alteration in AD pathogenesis (Extended Data Fig. 1a-c). Using in silico modeling, we first confirmed the stability of both Aβ residues (40 and 42) with Discovery Studio, which analyzed the docked structure for binding poses. Methylglyoxal can interact with both Aβ fibrils, but 42 residues bind more strongly (binding energy -2.6) than 40 residues (binding energy -2.2) (Extended Data Fig. 1a, b). Formation of glycated Aβ (with $Aβ_{42}$) was further validated with a fluorescence spectrophotometer measuring AGE-specific fluorescence at an emission of 450 nm and excitation of 350 nm (Extended Data Fig. 1c). We observed higher gAβ plaques and AGE levels, as well as increased Aβ and AGE colocalization in the hippocampal (Fig. 1a). and cortical region (Fig. 1b, c) of human AD samples relative to age-matched controls. We also confirmed a higher expression of RAGE in cortical regions of human AD samples (Fig. 1d). In addition, we found higher levels of cytoplasmic mtDNA in AD hippocampus compared to age-matched controls, despite having similar levels of total mtDNA (Fig. 1e, f). More importantly, the innate immune cGAS-STING pathway was significantly enhanced in the cortical region of human AD patients (Fig. 1g, h), as immunostaining data confirmed increased levels of cGAS and phosphorylated STING (pSTING) in neurons of AD hippocampus, surprisingly, almost no pSTING expression in neurons was observed in tissue from aging controls (Extended Data Fig. 1d, e), in line with the notion that STING is normally found in microglia[23]. To verify whether cGAS binds to mtDNA in the cytosol, we performed ultra-sensitive Proximity ligation assay (PLA) in which a signal is only produced if the two proteins are closer than 40 nm. PLA results showed an over 8-fold increase in cGAS-dsDNA binding in the AD hippocampus compared to controls (Fig. 1i, j). Our data also revealed much higher levels of inflammatory cytokines, including TNF-α, IL-1β and IL-6, in the cortical region of AD samples (Extended Data Fig. 1f), which is consistent with the activation of cGAS-STING and downstream type I IFN pathway[11]. Fission and fusion proteins are crucial for preserving the health and function of mitochondria[24-26]. Our immunoblot data confirmed increased levels of dynamin-related protein 1 (Drp1) and its phosphorylated form (pDRP1), and reduction in mitofusin-1 (Mfn-1) and mitofusin-2 (Mfn-2) in cortical AD brain samples compared to age matched controls (Extended Data Fig. 1g), confirming that mitochondrial dynamic changes in AD. Our data also revealed increased generation of reactive oxygen species (ROS), defective glycolytic and mitochondrial function, and an energy imbalance in AD tissue (Extended Data Fig. 1h-o). Next, we prepared cytosolic and mitochondrial fractions from cortical tissues from AD and age-matched controls and found much higher levels of cytochrome c (Cyt c) in the cytosolic fraction in AD brains (Fig. k-l), while Cyt c level in the mitochondrial fraction was higher in controls (Fig. l). More importantly, we confirmed higher oligomeric expression of VDAC1 in AD brains (Fig. 1n,

o), confirming the link between gAβ load in AD with mitochondrial dysfunction and voltage-dependent anion channel 1 (VDAC1)-dependent macropore facilitation for Cyt c release, and cGAS-STING activation in neurons.

Aβ glycation exacerbated neuronal mitochondrial stress and neuroinflammation *in vitro*

We next sought to determine if pathogenic gAβ (i.e., $A\beta_{42}$-AGE) activates cGAS-STING signaling in neurons and induces neuroinflammation. We cultured primary hippocampal neurons that were treated with human Aβ (i.e., $A\beta_{42}$) or gAβ (i.e., $gA\beta_{42}$). As previously reported[27] RAGE level was increased after Aβ treatment, but we found that gAβ had much stronger effect in upregulating RAGE in cultured primary neurons (Fig. 2a). Next, we showed that gAβ induced stronger activation of the cGAS-STING pathway, based on the increased levels of cGAS, pSTING, STING, p-TBK1, and p-IRF3 in gAβ-treated neurons relative to Aβ or vehicle (Fig. 2b, c), which was consistent with the fact that the highest cytoplasmic mtDNA level was also seen in gAβ treated neurons (Fig. 2d, e). The substantial upregulation of cGAS in gAβ treated neurons was further validated by immunocytochemistry (Fig. 2f). We also detected increased production of 2′3′-cGAMP by cGAS, in both Aβ and gAβ-treated primary neurons (Fig. 2g), and the level in the gAβ-treated condition was higher than Aβ condition. In examining the consequence of the activation of the cGAS-STING pathway, we found a marked increase in the IFN-β level in the culture media secreted by the neurons treated with gAβ (Fig. 2h), as well as much higher levels of inflammatory cytokines (TNF-α, IL-1β, and IL-6) in gAβ-treated neurons (Extended Data Fig. 2a, b). These results suggest that both Aβ and gAβ can induce broad activation of cGAS in neural cells, but gAβ can more specifically trigger STING-IFN responses in neurons.

To determine whether gAβ disrupts mitochondrial function, we assessed mitochondrial respiratory function and energy metabolism by measuring the activity of mitochondrial respiratory chain complexes I, IV and, ATP levels in vehicle, Aβ or gAβ treated neurons. Compared to vehicles or Aβ, gAβ induced significantly suppressed the activity of complex I and IV in neurons (Extended Data Fig. 2c, d). In parallel, neuronal mitochondria had reduced ATP levels in the presence of gAβ (Extended Data Fig. 2e), suggesting gAβ induced most severe impairments in mitochondrial respiratory function and energy metabolism. Altered glycolysis can also impair mitochondrial metabolism[28], and we found that gAβ treated neurons exhibited DHAP upregulation and G3P downregulation (Extended Data Fig. 2f, g). Our immunoblot analysis further demonstrated a higher expression of phosphorylated Drp1 (pDrp1) and a decrease of MFN-2 in gAβ treated neurons when compared to vehicle or Aβ, confirming mitochondrial dynamic changes can be directly induced by gAβ (Extended Data Fig. 2h-j). Since mitochondrial membrane potential controls matrix configuration and Cyt c release during apoptosis[29], we analyzed it with Tetramethylrhodamine Methyl Ester (TMRM) and FACS. Remarkably, our data confirmed diminished TMRM levels in gAβ-treated neurons compared to Aβ or vehicle (Extended Data Fig. 2i, l).). Mitochondria are the main source of ROS. Thus, we determined whether gAβ elevates oxidative stress in neurons. As shown (Extended Data Fig. 3a), gAβ-treated neurons had significantly more H_2O_2 than vehicle or Aβ condition. Furthermore, FACS analysis confirmed increased level of ROS in gAβ-treated neurons compared to Aβ or vehicle (Extended Data Fig. 3b, c). Consistent with these observations, we quantitatively measured intracellular ROS levels in primary neurons treated with Aβ/gAβ by highly specific EPR spectroscopy. The intracellular ROS levels indicated by EPR peaks were significantly elevated in Aβ and gAβ-treated neurons compared to vehicle-treated neurons; however, the generation of ROS was more robust in the gAβ-treatment condition compared to Aβ-treated neurons (Extended Data Fig. 3d, e). Additionally, we observed higher expression of VDAC1 in gAβ-treated neurons (Fig. 2i). It is worth noting that Aβ treatment had very little or no effect on VDAC1 (Fig 2j).

To analyze whether gAβ and cGAS-STING activation exacerbate neurotoxicity, we

cultured mature mouse neurons with vehicle, Aβ or gAβ treatment, and used microtubule-associated protein 2 (MAP2) as a dendritic marker, and synaptophysin and GluR1 as presynaptic and postsynaptic markers, respectively (Fig. 2k). Both Aβ and gAβ treated neuronal dendrites not only showed diminished length of dendrites, but also reduction in GluR1- or synaptophysin-positive clusters (Fig. 2k-n). Remarkably, gAβ had a most deleterious effect on dendrites length and synaptic density compared to vehicles or Aβ treated neurons (Fig. 2l-n). Furthermore, to understand gAβ-induced STING-IFN response in inducing specific neuroinflammation and molecular signatures, we analyzed RNAs from the vehicle, Aβ or gAβ-treated neurons using the amplification-free nCounter neuropathology profiling panel from NanoString. Twenty-nine genes including *Calr*, *Dlg4*, *Egr1*, *Gja1*, *Gria2*, *Mapt*, *Nlgn2*, *Nrgn*, *Plekhb*, *Slc17a7*, *Slc1a3*, *Syn2*, *Syp*, and *Tubb3* out of eighty genes associated with neuropathology were highly expressed in gAβ-treated neurons compared to vehicle or Aβ-treated neurons (Extended Data Fig. 3f). This data validates that gAβ can cause mitochondria dysfunction and mtDNA release, and trigger cGAS-STING activation and inflammation in neurons.

Increased Aβ glycation in APP mice induced mtDNA leakage and cGAS-STING activation

We next determined if Aβ glycation exacerbates neuronal mitochondrial dysfunction and AD pathogenesis *in vivo*. There was a higher level of methylglyoxal (AGE precursor) along with amyloid beta (Aβ42 and Aβ40) level in APP mice at 8 months of age compared to nonTg controls (Extended Data Fig. 4a-c). At this age, RAGE expression was also significantly increased in brain cells of APP mice compared to controls (Extended Data Fig. 4d). Next, we confirmed that Aβ in the senile plaques of APP mice was highly glycated by immunofluorescence staining (Fig. 3a). Complex of Aβ and AGE (gAβ) from cortical tissues of 3, 6, and 8-month-old APP mice further confirmed age-dependent Aβ glycation in APP mice (Extended Data Fig. 4e). As mtDNA often binds with TFAM (transcription factor A, mitochondrial)[30], we isolated and characterized cytosolic and mitochondrial fractions of brain cells in 8-month-old nonTg and APP mice (Extended Data Fig. 4f), and found TFAM proteins were present in the cytosolic fraction from APP mice (Fig. 3b-c). APP mouse also had much higher levels of cytosolic mtDNA compared to nonTg mice (Fig. 3d), despite the similar levels of total mtDNA (Fig. 3e). This mtDNA leakage associated with gAβ and plaques stress is also age-dependent, as 3- and 6-month-old APP mice showed relatively lower quantities of cytoplasmic mtDNA (Extended Data Fig. 4g-h).

The mtDNA efflux to the cytosol can be sensed by cGAS and lead to STING activation. We first confirmed that neuronal cGAS expression was significantly increased in APP mice compared to age-matched controls by immunofluorescent staining and immunoblots (Fig. 3f-h). Immunoblotting assay showed that cGAS, STING, and phosphorylation levels of STING (p-STING), TBK1 (p-TBK1), IRF3 (p-IRF3) were all significantly enhanced in the hippocampal region of 8-month-old APP mice, compared to age-matched nonTg controls (Fig. 3g, h), although it was less robust in younger 3 and 6-months-old APP mice indicating its dependence on aging (Extended Data Fig. 4i, j). PLA analysis on brain hippocampal tissues from 8-month-old APP mice showed an over 6-fold increase in cGAS-dsDNA interactions when compared with nonTg controls (Fig. 3i, j). Moreover, it was more robust in the hippocampus area of 8-months old APP mice than 3 and 6-months old (Extended Data Fig. 4k, l). In contrast to their nonTg littermates, APP mice exhibited increased levels of pSTING in their neural cells (Fig. 3k). In addition, the upregulated level of IFN-β was observed in 8-month-old APP mice hippocampus compared to nonTg controls and increased over aging (Fig. 3l; Extended Data Fig. 4m).

Next, we also performed neuroinflammation bulk gene expression analysis from cortex of 8-month-old AD mice. In the comparison between APP and nonTg mice, we identified significant changes in 133 genes: 106 were upregulated and 27 downregulated (Extended Data Fig. 4n).

Pathway analysis identified several neuroinflammatory activities, including ‘‘cytokine signaling, innate immune response, apoptosis, carbohydrate metabolism, neuropathology, microglial function, DNA damage, inflammatory signaling, cellular stress and astrocyte function’’ (Extended Data Fig. 4o), suggesting a global change in the immune status in this APP knock-model, which is associated with gAβ and cGAS-STING activation. STING is expressed in the brain with highest level in microglia, but it also exists in neurons. More evidence also supports its presence in iPSC-derived neurons[31].

Knockdown of RAGE, cGAS, or STING attenuated mitochondrial dysfunction, mtDNA and cytochrome c release

To further verify the role of RAGE in gAβ-induced cGAS-STING activation, target-specific shRNA in adeno-associated viral vector (AAV) was administrated in 7-months-old APP mice through intracerebroventricular injection (ICV) to silence RAGE, cGAS, or STING in the CA1 region of both hippocampi (Extended Data Fig. 5a). Immunoblot data confirmed the efficacy of shRNA AAV delivery and silencing of RAGE, cGAS, and STING (Extended Data Fig. 5b-e). The knockdown of RAGE mimicked the cGAS or STING inhibition, and suppressed the activation of cGAS, pSTING, STING, pIRF3 and pTBK1 in the hippocampal CA1 region of APP mice administrated with AVV-shRNA (Fig. 4a, b). Immunofluorescence results also demonstrated that RAGE, cGAS, and STING knockdown decreased cGAS expression in neurons of the hippocampal CA1 region of APP mice (Fig. 4c). PLA analysis confirmed the substantial reduction of cGAS-dsDNA interaction in the CA1 region of the hippocampus in APP mice following cGAS and RAGE knockdown (Fig. 4d, e)**.** Interestingly, immunoblot data confirmed mitochondria stress was only relieved in RAGE-knockdown APP mice as shown by reduction of Cyt c in the cytosolic fraction (Fig. 4f-h), but in cGAS or STING knockdown conditions, indicating gAβ-induced mitochondria dysfunction is dependent on RAGE and upstream of cGAS-STING activation. Likewise, we also observed a considerable drop in TFAM in the cytosolic fraction (Fig. 4f, i), and restoration of mitochondrial respiration and ATP levels (Extended Data Fig. 5f-h), only in APP mice with RAGE knockdown. In parallel observation, the levels of DHAP and G3P were improved in RAGE knockdown APP mice (Extended Data Fig. 5i, j)**,** intracellular ROS levels as indicated by EPR peaks were significantly reduced in RAGE knockdown APP mice (Extended Data Fig. 5k, l)**.** These data indicate that RAGE is linked to mitochondrial dysfunction and cGAS-STING activation.

Next, we used multiplexed gene expression analysis (NanoString nCounter) to investigate gene expression changes in relation to RAGE, cGAS, and STING knockdown in the APP mice. Twenty-nine differentially expressed genes associated with neuropathology, including *Akt1, Akt2, Apoe, Bdnf, Creb1, Igf2r, Gria2, Mapt, Syn2, Syp,* and *Tgfa* (Extended Data Fig. 6a); eighteen associated with astrocyte function, including *Clcf1, C4a, S100b, Slc1a3*, and *Tm4sf1* (Extended Data Fig. 6b); and thirty-eight associated with microglial function, including *Atp6v1a, Bnip3, Cox6b, Il10rb, Il1b, Map2k1, Optn, Tnf*, and *Trem2* (Extended Data Fig. 6c), were consistently downregulated in RAGE, cGAS or STING knockdown mice compared to controls. We also observed twenty-nine differentially expressed genes associated with innate immune response, including *Bcl2l1, Ciqa, C1qb, C1qc, Ifnar1, Ifnar2, Irf1, Irf2, Irf3, Irf7, Mapk10, Nfkb1*, and *Tbk1* (Extended Data Fig. 6d); seventeen genes associated with DNA damage, including Abl1, Apex1, Bax, Cdkn1a, Fen1, Kdm4b, Pten, Pttg1, and Rp1a (Extended Data Fig. 6e) and thirteen genes associated with cellular stress, including *Anapc15, Atg14, Atg7, Atg9a, Ehmt2*, and *Hdac2* control (Extended Data Fig. 6f), downregulated in RAGE, cGAS or STING knockdown APP mice. Among the inflammation-related proteins in our correlation matrix expression panel of all samples, DNA damage was highly linked with neurons and neurotransmission, compared to other pathways or cell types (Extended Data Fig. 6g), further

demonstrating that DNA damage is a driving force of neuronal dysfunction in the APP model. At the confluence of innate immunity and DNA damage, cells mount an innate immune response in response to foreign DNA that is introduced into the cytoplasm.

VDAC1 inhibition restrained mtDNA leakage, cGAS-STING pathway and cognitive decline

Formation of mitochondria macropores, including Voltage-dependent anion channel (VDAC) oligomers, Bcl2-associated X protein (BAX) / Bcl2 killer (BAK) macropore, and Cyclophilin D (CypD)-containing mitochondrial permeability transition pore (mPTP), facilitates mitochondrial herniation and mtDNA efflux. To explore the molecular mechanism behind the mtDNA release and cGAS-STING activation, we administrated NSC15364, BIP-V5, or Cyclosporin A (CsA) in 6.5-month-old APP mice (Extended Data Fig. 7a) to pharmacologically inhibit VDAC1, BAX or CypD respectively[32-34]. CsA or NSC15364 but not BIP-V5 restored mPTP function, and CsA-administered APP mice mitochondrial were more resistant to swelling and permeability transition induced by Ca^{2+} than NSC15364 (Extended Data Fig. 7b, c). However, CsA did not affect VDAC1 or BAK levels in the APP mice hippocampus (Extended Data Fig. 7d, e). Likewise, BIP-V5 treatment suppressed BAX and BAK expression and its oligomers but not CypD in APP mice hippocampus (Extended Data Fig. 7f, g). Our data also showed no changes in Cyt c expression in both fractions or mtDNA-binding protein TFAM expression in the cytosolic fraction after BIP-V5 treatment compared to vehicle-treated APP mice or nonTg control (Extended Data Fig. 7h-k). These data suggest that mtDNA efflux is unlikely dependent of BAX/BAK/CypD macropores.

Next, we verified that NSC15364, a VDAC1 oligomerization inhibitor, suppressed VDAC1 oligomerization and expression in APP or control mouses hippocampus (Extended Data Fig. 8a, b). Interestingly, our data also confirmed the inhibition of Cyt c leakage to cytosolic fraction under the treatment of VDAC1 inhibitor (Fig. 5a-c) compared to control, particularly in APP mice. Furthermore, immunoblot data proved a significant reduction of TFAM in cytosolic fraction in VDAC1 inhibitor-treated APP mouse hippocampal cells (Fig. 5a, d). Additionally, there was a significant reduction in cytosolic mtDNA in APP mouse brain cells treated with VDAC1 inhibitor, compared to the vehicle treated (Extended Data Fig. 8c-d). Furthermore, immunofluorescence revealed colocalization of a flock of dsDNA with VDAC1 clusters in hippocampus of APP mice, which was repressed by the VDAC1 inhibitor NSC15364, validating VDAC1 oligomers dependent mtDNA release (Fig. 5e, f). Immunoblotting assay showed that cGAS, pSTING, STING, p-TBK1, and p-IRF3 were all significantly reduced in the hippocampal region of 8-month-old APP mice after NSC15364 treatment, compared to vehicle treated groups (Fig. 5g, h). Additionally, PLA assay confirmed a significant inhibition of dsDNA and cGAS interaction in VDAC1 inhibitor administered APP mice hippocampus compared to vehicle treated (Fig. 5i, j). Our immunofluorescence observations also proved that the VDAC1 inhibitor NSC15364 blocked cGAS upregulation in APP mice hippocampal neurons compared to vehicle-treated (Fig. 5k). Moreover, VDAC1 inhibition by NSC15364 not only effectively inhibited cGAS-STING pathway and production of inflammatory mediators such as TNF-α, IL-6 and IL-1β (Fig. 5l-n), but also oxidation of mtDNA[35] (Extended Data Fig. 8e).

In addition to affecting signaling cascades, gAβ may influence the plasticity of hippocampal circuits, e.g., long-term potentiation (LTP). We used electrophysiology in acute slice preparations to analyze field excitatory postsynaptic potential (fEPSP) and assess possible changes in the capacity for plasticity of hippocampal neurons treated with gAβ. Theta burst stimulation (TBS) induced comparable post-tetanic potentiation of fEPSPs in slices pre-incubated with vehicle, Aβ, or gAβ (Extended Data Fig. 8f-j). However, the magnitude of LTP, measured 40-60 min following induction, was significantly reduced with either Aβ or gAβ treatment, when compared with vehicle group (Extended Data Fig. 8i, j), indicating impaired hippocampal plasticity in the presence of Aβ or gAβ.

Given the vital role of mitochondria in generating the energy necessary for neuronal functions[36], we next assessed whether VDAC1 inhibitor can restore neuronal function in APP mice. To assess spatial learning and memory, vehicles or NSC15364 administered mice were tested on the Morris Water Maze (MWM) test. Compared to vehicle administered nonTg mice, APP mice displayed significantly longer escape latencies during the 5-day training session (Fig. 5o) and reduced number of crossings of the target area and time spent in the target quadrant during the probe trial (Fig. 5p, q), which were significantly improved with NSC15364 treatment (Fig. 5o-q). There were no significant differences in swimming speed as measured by the visual swimming speed test in all groups **(**Fig. 5r**)**, indicating that the observed difference in spatial learning and memory is due to cognitive decline rather than differential motility or motivation. In addition, daily task performance was measured by assessing mouse nest-making ability[37]. Vehicle-administered APP mice scored significantly lower on the nestlet task compared to nonTg mice, and NSC15364-administered mice showed significant improvement on the nestlet task **(**Fig. 5s**)**, suggesting that administration of VDAC1 inhibitors could lead to improvement in daily task performance in AD.

RAGE inhibition averted cGAS-STING activation and cognitive decline in APP mice

To further illustrate the role of RAGE in cGAS-STING signaling in AD, we administered Azeliragon (a RAGE inhibitor, formerly TTP488) in 6.5-months-old APP mice for six weeks (Extended Date Fig. 9a). Our immunoblot data confirmed that treatment with Azeliragon not only effectively attenuated cGAS and STING but also reduced the phosphorylation of cGAS-STING pathway proteins (pSTING, pTBK1, pIRF3) (Fig. 6a, b). In addition, we observed decreased levels of presynaptic synaptophysin and postsynaptic PSD-95 proteins, reflecting synaptic disruption in the APP mice. Importantly, there was a significant restoration of synaptophysin and PSD95 in the hippocampus of Azeliragon-treated APP mice (Fig. 6c, d). Moreover, PLA assay confirmed a significant inhibition of dsDNA and VDAC1 interaction in Azeliragon administered APP mice hippocampus compared to vehicle treated (Fig. 6e, f). Our immunofluorescence observations further proved that the Azeliragon blocked cGAS expression in APP mice hippocampal neurons compared to vehicle-treated (Fig. 6g). The ability to construct mouse nests was used to gauge daily task performance. Azeliragon-administered APP mice show remarkable improvement on the nestlet task compared to vehicle administered mice **(**Fig. 6h). Next, to assess spatial learning and memory, APP mice were subjected to MWM test. Compared to vehicle administration, APP mice treated with Azeliragon displayed significantly lower escape latencies during the 5-day training session (Fig. 6i) and an increased number of crossings of the target area, as well as time spent in the target quadrant during the probe trial (Fig. 6j, k), while swimming speed was very similar in both groups (Fig. 6l**)**.

To survey the RAGE-mediated transcriptomic changes in APP mice, we profiled the coronal brain section by Stereo-seq, which is an in situ sequencing technology using DNA nanoball-patterned arrays (DNB) on lithographically etched chips[38,39], (Extended Date Fig. 9b). These included the cortex and subcortical regions such as hippocampus, thalamus, and striatum, among others (Extended Date Fig. 9c, d). These regions included neurons as well as non-neuronal cells (Extended Date Fig. 9e). We applied image-based cell segmentation that enabled accurate integration of transcript images into an image-guided gene by-cell matrix. We then validated the effect of RAGE inhibitor on regulating the clustering of AD associated gene by-cell matrix and subsequent detailed annotation based on the expression of marker genes that identified different types and subtypes of cells, which included voltage-dependent anion channel (VDAC1, VDAC2, VDAC3, VDAC3-PS1; Extended Date Fig. 9f), innate immunity (*Irf2, Irf3, Ifnar2, Ifnar1, TMEM173, Irak1, Irf9*; Extended Data Fig. 9g), neuropathology (*Mapt, Syp, Arc, Plekhb1, Homer1, Slc17a6, Syn2*; Extended Data Fig. 9h), A1 astrocyte (*Tnfaip1, C1qa, C1qb,*

C1qc, Fkbp5, Serping1, C1qTnf12; Extended Data Fig. 9i), disease-associated microglial (*Trem2, IgF2, Lyn, Apoc1, Ctsz, Cd52, Cd9*; Extended Data Fig. 9j), cytokine signaling (*Cx3cl1, Tnfsf12, IL10rb, Nfkbib, IL6, IL2, Tnfrsf21*; Extended Data Fig. 9k), DNA damage (*BAX, VDAC1, TBr1, Lingo1, Pttg1, CD83, BAK1*; Extended Data Fig. 9l), cellular stress (*Prdx1, Nqo1, Anapc15, Srxn1, Hira, Hdac2, Ambra1*; Extended Data Fig. 9m) and apoptosis related genes (*Cidea, Bcl2l2, Bcl2, Bcl2l1, Bcl10, Map2k4, Ikbkg*; Extended Data Fig. 9n). The special location of the different cell types was also consistent with existing knowledge of the corresponding anatomic regions annotated using bins. Additionally, stereo-seq showed inhibition of the stated MID count disease-associated gene in Azeliragon-administered APP mice compared to vehicle control, suggesting the relation between RAGE and the innate immune response in AD. Thus, RAGE inhibitor may block gAβ-induced VDAC1 oligomerization and cGAS-STING sensing apoptotic pathways.

Discussion

Evidence has been presented that Aβ is a stable and suitable substrate for glycation[40]. gAβ is one form of AGEs and is more prone to bind to/activate RAGE than authentic Aβ. The plaques in AD brains are highly colocalized with AGEs and are enriched with AGE adducts, implying that Aβ is glycated. However, the role of gAβ in AD pathogenesis was still unclear. Hereby, we verified that Aβ glycation leads to neuronal mitochondrial dysfunction and Alzheimer's pathogenesis via VDAC1-dependent mtDNA efflux, as shown by the schematic signaling transduction pathway (Extended Data Fig. 10). After binding to RAGE, gAβ can induce neuronal mtDNA efflux dependent on VDAC1, activating the cytosolic cGAS-STING sensing pathway in AD. Cytosolic cGAS-mtDNA binding in neuron then triggers STING pathway activation in aged AD mice and human AD brains, resulting in neuroinflammation and neurodegeneration. Knockdown of RAGE, cGAS, or STING largely protected APP mice from mitochondrial dysfunction and AD-like pathology, so did pharmacological inhibition of VDAC1. Furthermore, inhibition of RAGE in APP mice, coupled with in situ RNA capture using spatially enhanced resolution omics-sequencing, confirmed the downregulation of innate immune response and disease associated genes in AD. Thus, our study identifies a crucial molecular link between gAβ and innate immunity in neurons, suggesting that therapeutic targeting of mitochondrial VDAC1, RAGE, or cGAS-STING may enhance resilience against gAβ-related pathological insults in AD.

Cytosolic mtDNA leakage with subsequent cGAS-STING activation in AD has been confirmed in microglia consistent with the notion that STING is highly expressed in microglia. Interestingly, we found that STING is also highly expressed in the neurons of AD patients and APP mice but not in normal control counterparts, suggesting neuronal STING is only expressed under stress, in line with earlier reports that STING can also be detected abundantly in neurons under certain conditions. Previous studies found the STING-IFN cascade was present mainly in microglia[41-43]; however, our results raise the question of how the signal of cGAS sensing dsDNA within neural cells is transduced to the activation of the microglial STING-IFN cascade. By RNA-sequencing, we postulated that the activation of the IFN response was only present in gAβ-stressed neurons but not authentic Aβ. It is suggested that directly activating neuronal STING by cGAMP promotes axon regeneration and can be transported between neighboring cells via specific transporters and gap junctions[44,45]. Consistent with this, we proposed that DNA binding cGAS in gAβ-stressed neurons undergoes phase separation and generates the 2'3'-cGAMP, which not only translocate from the ER towards the ER-Golgi intermediate compartment to activate STING in neurons but also astrocytes and microglia and subsequently induces the activation of the STING-IFN cascade, thereby stimulating/amplifying neuroinflammatory responses.

RAGE contributes to AD pathology, in part, by being involved in the translocation of gAβ

from the extracellular to the intracellular space and transported into *mitochondria* via the translocase of the *outer membrane* (TOM), thereby enhancing gAβ cytotoxicity via mitochondrial dysfunction[46]. Remarkably, through mitochondrial VDAC1 expression and homo-oligomerization mitochondrial pores, mtDNA is released into the cytosol in response to pathogenic stimuli[47,48]. We found that only gAβ, not authentic Aβ, can induce mtDNA efflux in neurons, which is dependent on VDAC1. We presented the first evidence of VDAC1 directly causing mtDNA efflux in an amyloidogenic mouse model.

We show a connection between gAβ-RAGE and cGAS-STING sensing, and mitochondrial dysfunction. Our work provides a mechanistic description of VDAC1-mediated mtDNA release under gAβ and subsequent mitochondrial stress/apoptosis, which represents one of the innate immune cGAS-STING activations. Future research is necessary to better understand how the neurodegenerative changes are modulated by innate or adaptive immunity and whether these detrimental effects on neuronal function can be partially or even completely reversed.

Methods

Human tissues

Post-mortem frozen and paraffin embedded human brain samples were obtained from the Case Western University Reserve University, School of Medicine, Cleveland, Ohio. The postmortem interval (PMI) was < 9 hr. Informed consent was obtained, and the study approved by the Institutional Review Board of Case Western Reserve University, Cleveland, Ohio. All autopsy cases underwent neuropathological evaluation of AD including assignment of Braak stages. Aged subjects that did not carry diagnosis of AD or another neurodegenerative disease and showed neuropathological findings within the normal range for age were used as age-matched controls. The brain samples were quickly frozen and used for immunoblotting analysis. In addition, brain tissues were fixed and embedded into paraffin and 5-μm thick consecutive sections on silane-coated slides were used for immunohistochemistry. The demographic information of all cases is provided in Supplementary Table 1. All procedures performed in this manuscript were in accordance with the ethical standards of Case Western Reserve University, Cleveland, Ohio.

Mice

Mouse studies were approved by the Animal Care and Use Committee of ST. University in accordance with the US National Institutes of Health guidelines for animal care. The App knock-in mouse model (App^{SAA} KI/KI; B6.Cg-Apptm1.1Dnli/J, Jackson Lab # 034711) of Alzheimer's disease (AD) was used which carries humanizing Aβ region R684H, F681Y, and G676R mutations, and the KM670/671NL (Swedish) mutation in exon 16 as well as the E693G (Arctic) and T714I (Austrian) mutations in exon 17 of the mouse *App* (amyloid beta (A4) precursor protein) gene. Mice recapitulate amyloid plaque pathology *in vivo* without disturbing intrinsic gene expression. Both male and female were used throughout the study. The 7-months old App^{SAA} (APP) mice were used for RAGE-shRNA, cGAS-shRNA, TMEM173-shRNA and scrambled intracerebroventricular injection. The 6.5-month-old APP mice were intraperitoneally (i.p.) injected with Bcl-2-associated X protein (BAX), voltage-dependent anion channel (VDAC), Cyclophilin D (CypD) or RAGE inhibitor i.e., BIP-V5 (5 mg kg−1 BW; 10% DMSO + 40% PEG300 + 5% Tween-80 + 45% saline; HY-P0081, MCE), NSC 15364 (2.5 mg kg−1 BW; 10% DMSO + 40% PEG300 + 5% Tween-80 + 45% saline; Cat #HY-108937, MCE), Cyclosporin A (CsA) (1 mg kg−1 BW i.p. 5% DMSO 40% PEG300 5% Tween-80 50% saline; Cat #HY-B0579, MCE) twice each week, and Azeliragon (100 mcg; 10% DMSO 40% PEG300 5% Tween-80 45% Saline; Cat #HY-50682, MCE) every day for 6 weeks. The solvent of the inhibitor was used

as vehicle control with the same volume for i.p. injection for 6.5-month-old APP mice. Animals were maintained in facilities with a 12-h light–dark cycle, an average ambient temperature of 21°C, an average humidity of 48% and had free access to food and water. The Institutional Animal Care and Use Committee of Stony Brook University approved all experimental procedures and protocols. All guidelines for research with animals were adhered to during this study.

Docking study

The structure of amyloid beta fibril (40 and 42 residues) was obtained from the protein data bank using the PDB IDs 2M4J (40 residues) and 8eze42 (42 residues). The PubChem database was accessed to find the 3D Conformer of Methylglyoxal (MGO). These structures were prepared for docking analysis using Discovery Studio 2021, and the prepared Methylglyoxal was docked with both the structure (40 and 42 residues) of amyloid beta fibril using Autodock 4.2.

Glycated amyloid beta (gAβ) preparation

Glycated Aβ (gAβ) was prepared by incubating 10 mg/ml of human Aβ1-42 (Sigma-Aldrich) with or without 0.5 mM methylglyoxal (MGO) in 0.1 M phosphate buffer, pH 7.2, at 37ºC for three weeks under sterile conditions. After dialysis against phosphate buffer for 48 h at 4ºC to remove MGO, the prepared glycated Aβ (gAβ) was sterilized by filtration and kept at -20ºC in aliquots. The production of gAβ was identified with a fluorescence spectrophotometer measuring AGE-specific fluorescence at an emission of 440 nm and excitation of 370 nm (Perkinelmer, Waltham, MA, USA).

Primary neuron cell cultures

Mouse pups (P0) were decapitated. Hippocampi removed by micro-dissection were trypsin-treated (0.25%) and triturated before plating in high glucose DMEM (10% fetal calf serum) (Invitrogen) onto glass cover slips coated with poly D-lysine (20 µg/mL) (Sigma-Aldrich) (Invitrogen), as described. Cells were maintained in an incubator at 37ºC with 5% CO_2. The next day, the medium was replaced with Neurobasal A medium supplemented with 2% B27 and 2 mM GlutaMAX (Life Technologies). Cells were then stored in the incubator for 10 DIV followed by replacement of half of the medium with fresh B27-Neurobasal A medium containing 2µM Aβ or 2µM gAβ or vehicle which were kept for 24 hours.

Production of AAV9-RAGE/TMEM173 construct

Viral production and packaging using recombinant adeno-associated virus type 9 (rAAV9) encoding a protein of interest under control of the type III RNA polymerase III (U6) promoter (Vector Biolabs). Briefly, AAV-GFP-U6-shRNA plasmids were co-transfected into HEK293 cells with pAdhelper and AAV9-RC plasmid. 2 days after transfections, cell pellets were harvested, and viruses were released through 3x cycles of freeze/thaw. Viruses were purified through CsCl-gradient ultra-centrifugation, followed by desalting. Viral titer (GC/ml - genome copies/ml) are determined through real-time PCR.

Short hairpin RNA (shRNA) Intracerebroventricular Injection and cell transfection. RAGE small hairpin RNA (shRNA) (AAV9-GFP-U6-m-TMEM173-shRNA, target sequence: AGCTGGCACTTAGATGGGAAACTTCAAG AGAGTTTCCCATCTAAGTGCCAGCT), cGAS shRNA (AAV9-GFP-U6-m-TMEM173-shRNA, target sequence: GAGCTACAAGAATATTATGAAATTCAAGAGATTTCATAATATTCTTGTAGCTC) and STING shRNA (AAV9-GFP-U6-m-TMEM173-shRNA, target sequence: CAACATTCGATTCCGAGATATT TCAAGAG AATATCTCGGAATCGAATGTTG) were used in

our experiments. The RAGE, cGAS, STING and scrambled shRNA (AAV-GFP-U6-shRNA) were synthesized by Vector Biolabs (Pennsylvania, USA). Male and female APP mice at 7-month of age were anesthetized with an intraperitoneal (IP) injection of a cocktail containing 100mg/kg ketamine and 10mg/kg xylazine. Bupivacaine (2.5mg/ml, ~0.1mL) was administered under the scalp for local anesthesia. Craniotomies were made over the left and right CA1 at the following coordinates: -2.0mm posterior from Bregma, 1.1mm and 1.5mm lateral from midline (2 separate injection sites/side). A pulled glass pipette was attached to a nanoject pressure injector (Drummond nanoject II) and filled with shRNA virus (AAV9-GFP-U6-m-TMEM173-shRNA, AAV9-GFP-U6-m-TMEM173-shRNA and AAV9-GFP-U6-m-TMEM173-shRNA). The pipette was lowered 1.2mm below the pia. Approximately 1.0µl total volume was injected per side (0.5µl/injection site) over 10 minutes. The pipette tip was left in place at least 10min after the end of the injection. The skin was then sutured closed, and the animal recovered on a heating pad. Mice were then returned to their home cage and monitored. Vybrant Dil Cell-labeling Solutions (Thermo Fisher) was used to confirm the location of viral delivery.

Quantitative real-time PCR

Total RNA was extracted using a PureLink™ RNA Mini Kit (Thermo Fisher Scientific) according to the manufacturer's instructions. RNase free DNase (Promega) was used for DNase digestion during RNA purification. RNA quantity and quality were assessed by Nanodrop for RNA isolated from tissues. cDNA was generated from 1 µg total RNA per sample using the M-MLV Reverse Transcriptase kit (Promega). To detect RNA transcript of targeted genes, the target transcripts were determined by qPCR using the PereCTa SYBR Green SuperMix (Quanta Biosciences) on a CFX96 real-time PCR system (Bio-Rad).

Quantification of mtDNA release

Cultured primary neurons (2×10^6) or adult mouse brains both hippocampi were resuspended in 170µl of digitonin buffer containing 150 mM NaCl, 50 mM HEPES, pH 7.4 and 25µg/ml digitonin (Millipore Sigma). The homogenates were incubated on a rotator for 10 min at room temperature, followed by centrifugation at 16,000g for 25 min at 4°C. A 1:20 dilution of the supernatant (cytoplasmic mtDNA) was used for qPCR. The pellet was resuspended in 340µl of lysis buffer containing 5 mM EDTA and proteinase K (Qiagen) and incubated at 55°C overnight. The digested pellet was diluted with water (1:20 to 1:100) and heated at 95°C for 20 min to inactivate proteinase K and the sample was used for qPCR with mtDNA-specific primers (*Dloop1*, *CytB* and *Nd2*) listed in Supplementary Table 2.

NanoString nCounter gene expression

For neuropathology, disease-associated microglial function, activated astrocytes, innate immune responses, DNA damage, and cellular stress-related gene analysis (listed in Supplementary Table 3), NanoString Mouse neuroinflammation panels were used (NanoString Technologies). RNA was extracted from either the primary cell (neuronal, astrocytes, and microglia) or the CA1 region of the mouse brain hippocampus (CA1 region was poured from both hippocampi) using RNeasy Micro kits (Qiagen). RNA purity was confirmed by BioAnalyzer, and 100 ng/sample were hybridized with probes for 16 h at 65°C. The results obtained from the nCounter MAX Analysis System (NanoString Technologies, Seattle WA) were imported into the nSolver Analysis Software (v4.0; NanoString Technologies) for QC verification, normalization, and data statistical analysis using Advanced Analysis software (v2.0.115; NanoString Technologies). All assays were performed according to the manufacturer's protocols.

Immunofluorescence

PBS-perfused mice were fixed in 4% PFA overnight, followed by immersion in 30% (w/v) sucrose solution for 48 h and frozen with liquid N2. Samples were stored at −80°C prior to sectioning. The frozen brain was cryostat sectioned (coronal section) into 20 μm thick sections onto slides for histological staining. Sections were blocked for 1.5 h in PBST (containing 2% (w/v) BSA and 0.5% (v/v) Triton-X) followed by 1 h incubation with 0.5% (v/v) Mouse on Mouse (M.O.M.™) Blocking Reagent (Vector Laboratories). The primary antibodies above were diluted in 3% donkey serum in 1× PBST (0.2% Triton-X 100) and incubated overnight at 4°C. Slides were then washed, and immunoreactivity was detected using donkey anti-rabbit IgG Highly Cross-Adsorbed Secondary Antibody, Alexa Fluor Plus 488, donkey anti-Mouse IgG Highly Cross-Adsorbed Secondary Antibody, Alexa Fluor Plus 595 for 1 h at room temperature. The sections were mounted in SlowFade Gold Antifade Reagent with DAPI (Molecular Probes, Thermo-Fischer, Waltham, USA) and sealed by use of nail polish. Slides were visualized using a Zeiss LSM 980 Airyscan 2 NLO Two-Photon Confocal Microscope and then analyzed by ImageJ software. Detailed information of primary and secondary antibodies used are listed in Supplementary Table 4.

Immunoblotting

Protein samples were separated by SDS–PAGE and transferred to a nitrocellulose membrane (Amersham). The membrane was blocked in 5% skim milk in 1× PBST for 1 h and incubated overnight with primary antibody in 5% BSA at 4 °C. The membrane was incubated with anti-mouse or anti-rabbit HRP-conjugated secondary antibodies in 5% BSA and bands were developed with FluorChem imaging system (ProteinSimple). Immunoblot was also run by advanced western blot Abby (ProteinSimple) as per the kit instruction. All antibodies used are listed in Supplementary Table 4.

Proximity ligation assay

Binding of cGAS and cytoplasmic mtDNA in human and mouse brain sections was determined by a PLA kit (Sigma-Aldrich) according to the manufacturer's instructions. The primary antibodies used in PLA included anti-TFAM antibody (MA5-16148, Invitrogen), anti-cGAS antibody (human or mouse-specific, Invitrogen). PLA signals were visualized using a Zeiss LSM 980 Airyscan 2 NLO Two-Photon Confocal Microscope and indicated by PLA red dots per cell.

Isolation of mitochondria and cytosolic fraction

We isolated mitochondria from the hippocampus of Alzheimer's disease brains or hippocampus of mouse brains as described previously[49]. We used the highly purified mitochondria for immunoblotting and immunoprecipitation. For the mitochondrial function assay, mitochondria were isolated by centrifuging brain homogenates at 1,500g for 5 min at 4ºC. We adjusted the supernatant to 10% Percoll and recentrifuged at 12,000g for 10 min. We resuspended the mitochondrial pellet in the isolation buffer (225 mM D-mannitol, 75 mM sucrose, 2 mM K_2HPO_4, 5 mM HEPES, pH 7.2) containing 0.01% digitonin and recentrifuged at 6,000g for 10 min. We isolated cell mitochondria with a mitochondrial fractionation kit (Abcam). We determined protein concentration by the Bio-Rad DC protein assay (BioRad).

Mitochondrial swelling assay for mPTP

Calcium-triggered mitochondrial swelling assay was performed according to the method[50] with the modification. Mitochondria were isolated from the cortex of vehicle or drug treated (CsA or BIP-V5 or NSC15384) nonTg and Tg mice of 8 months old and suspended in 1 ml swelling assay buffer (500 μg protein, 150 mM KCl, 5 mM HEPES, 2 mM K_2HPO_4, 5 mM glutamate, 5 mM

malate, pH 7.2). $CaCl_2$ (100μM) is added into the mitochondrial suspension to initiate mitochondrial swelling at 540 nm of the spectrophotometer (Amersham Biosciences Ultrospect 3100). The total recording time was 12 minutes with a 30 second recording interval.

Enzyme-linked immunosorbent assay

Mouse hippocampus was extracted with guanidine (50 mM). Levels of cerebral Aβ40/42 were determined by ELISA according to the manufacturer's instructions (Invitrogen, CA). Furthermore, secretory IFN-β in supernatant and 2′3′-cGAMP in primary cells (neuron, astrocytes, and microglia) lysate after Aβ or gAβ treatment were quantified by mouse IFN-β (abcam) or mouse 2′3′-cGAMP ELISA kit (Cayman Chemical) according to the manufacturer's instructions. In addition, 8-hydroxy 2 deoxyguanosine (8-OhdG) in mouse brain cortical lysates (including hippocampus) was determined by competitive ELISA kit according to the manufacturer's instructions (abcam).

Glycerol-3-Phosphate (G3P), DHAP, and hydrogen peroxide (H_2O_2) in primary neuronal lysate after Aβ or gAβ treatment from mouse or human brain were quantified by the Glycerol-3-Phosphate Assay Kit (Sigma), High Sensitivity DHAP Fluorometric Assay Kit (Sigma), and Amplex™ Red Hydrogen Peroxide/Peroxidase Assay Kit (Invitrogen), respectively, according to the manufacturer's instructions.

Tetramethylrhodamine Methyl Ester Staining

WT hippocampal neurons from day 1 newborn mice at DIV 12 were treated with 1μM Aβ or 1μM gAβ or vehicle for 24 h for Tetramethylrhodamine methyl ester (TMRM) analysis by flow cytometry (CytoFLEX), as previously described [51].

Mitochondrial respiration complex activity

Mitochondrial respiration complex activity was measured using homogenates of the hippocampus or neuronal cells as previously described[52]. Briefly, hippocampus was homogenized, or cells were lysed in the isolation buffer containing 250 mM sucrose, 20 mM HEPES, pH 7.2, and 1 mM EDTA. Protein extracts (50μg) were used for complex I (COX I, NADH: ubiquinone oxidoreductase) and IV (COX IV, cytochrome c oxidase) assays. Complex I activity was determined by monitoring the change in absorbance at 340 nm every 20 s for 6 min. Complex IV activity was determined by cytochrome c reduction rate. Briefly, the protein samples were added to a cuvette containing 0.475 ml of assay buffer (10 mM Tris-HCL, pH 7.0, and 120 mM KCl), and the reaction volume was brought to 0.525 ml with enzyme dilution buffer (10 mM Tris-HCL, pH 7.0 and, 250 mM sucrose). The reaction was initiated by the addition of ferrocytochrome c substrate solution (0.22 mM) into the cuvette. The rate of change in absorbance at 550 nm was recorded using a kinetic program with 5 s delay and 10 s intervals for 6 readings using an Amersham Biosciences Ultrospect 3100 pro spectrophotometer.

Measurement of ATP levels

Adenosine 5'-triphosphate (ATP) levels were assessed using an ATP Bioluminescence assay Kit (Sigma/Roche). Briefly, mouse cortical tissues or neuronal cells were homogenized/lysed in the lysis buffer provided, incubated on ice for 30 min, and centrifuged at 12,000×g for 10 min at 4°C. ATP levels were then measured in the subsequent supernatants using a Luminescence plate reader (Molecular Devices). A 1.6 s delay time after substrate injection and 10 s integration time were used.

Mitochondrial Electron paramagnetic resonance (EPR) measurements

Evaluation of intracellular ROS levels was accessed by EPR spectroscopy[37]. Neurons or brain

tissues were incubated with CMH (cyclic hydroxylamine 1-hydroxy-3-methoxycarbonyl-2, 2, 5, 5-tetramethyl pyrrolidine, 100 μM) for 30 min, then washed three times with cold PBS. The brain tissues were collected and homogenized with 100 μL of PBS for EPR measurement. The EPR spectra were collected, stored, and analyzed with a Bruker EleXsys 540× -band EPR spectrometer (Billerica, MA, USA) using the Bruker software Xepr (Billerica, MA, USA).

In situ spatial resolve analysis (Stereo-sequencing)

It features a spatially resolved transcriptomic technology with high resolution and large field of view. Standard DNB chips have spots with approximately 220 nm diameter and a center-to-center distance of 500 or 715 nm (Extended Date Fig. 13a), providing up to 400 spots for tissue RNA capture per 100 mm^2. Frozen tissue sections (10mm thickness) are loaded on to the chip surface, followed by fixation, permeabilization to capture the tissue polyA-tailed RNA, and finally reverse transcription plus amplification. Amplified-barcoded cDNA is collected, used as template for library preparation, and sequenced together with the CID. Computational analysis of the sequencing data allows high-resolution spatially resolved transcriptomics known as spatial enhanced resolution omics-sequencing (Stereo-seq). To analyze the brain data, we performed unsupervised SCC of binned (bin 50, 50 x 50 DNB bins, 25 μm diameter) Stereo-seq data to identify the changes in disease associated MID count of genes with brain regions.

Generation of Stereo-seq chips. To generate the patterned array, we synthesized two oligo sequences: one containing 25 random deoxynucleotides DNB library oligo1 and the other a fixed sequence with 5' phosphorylated DNB library oligo2. These two oligos were ligated with splint oligo1 at 37°C for 2 hours using T4 ligase (NEB; 1U/ml T4 DNA ligase and 13 T4 DNA ligation buffer). The products were purified using the AMPure XP Beads (Vazyme, N411-03) and then PCR amplified with the following steps: 95°C for 5 minutes, 12 cycles at 98°C for 20 seconds, 58°C for 20 seconds, 72°C for 20 seconds and a final incubation at 72°C for 5 minutes. The PCR products were purified using the AMPure XP Beads. DNB were then generated by rolling circle amplification and loaded onto the patterned chips according to the MGI DNBSEQ-Tx sequencer manual. Next, to determine the distinct DNB-CID sequences at each spatial location, single-end sequencing was performed using a CID sequencing primer in MGI DNBSEQ-Tx sequencer with SE25 sequencing strategy. After sequencing, the capture oligo including 22 nt poly-T and 10 nt UMI was hybridized with the DNB in 5 x SSC buffer at 37°C for 30 minutes, and then incubated with T4 ligase (NEB, 1 U/ml T4 DNA ligase, 1 x T4 DNA ligation buffer and 0.5% PEG2000) at 37°C for 1 hour. This produces capture probes containing a 25 nt CID barcode, a 10 nt UMI and a 22 nt poly-T ready for poly-A RNA capture.

Calling of CID. CID sequences together with their corresponding coordinates for all DNB were determined using a base calling method according to manufacturer's instruction of MGI DNBSEQ-Tx sequencer. After sequencing, the capture chip was split into smaller size chips (5 mm x 10 mm, 10 mm x 10 mm, 10 mm x 20 mm) ready for use. At this stage, we filtered out all duplicated CID that correspond to non-adjacent spots.

Tissue processing. Mouse brain sections were adhered to the Stereo-seq chip surface and incubated at 37ºC for 3-5 minutes. Then, the sections were fixed in methanol and incubated for 40 minutes at -20C before Stereo-seq library preparation. Where indicated, the same sections were stained with nucleic acid dye (Thermo fisher, Q10212) and imaging was performed with a Ti-7 Nikon Eclipse microscope prior to in situ capture at the channel of FITC.

In situ reverse transcription. After washed with 0.1 3 SSC buffer (Thermo, AM9770)

supplemented with 0.05 U/ml RNase inhibitor (NEB, M0314L), tissue sections placed on the chip were permeabilized using 0.1% pepsin (Sigma, P7000) in 0.01 M HCl buffer, incubated at 37°C for 12 minutes and then washed with 0.1 3 SSC buffer (Thermo, AM9770) supplemented with 0.05 U/ml RNase inhibitor (NEB, M0314L). RNA released from the permeabilized tissue and captured by the DNB was reverse transcribed overnight at 42C using SuperScript II (Invitrogen, 18064-014, 10 U/ml reverse transcriptase, 1 mM dNTPs, 1 M betaine solution PCR reagent, 7.5 mM MgCl2, 5 mM DTT, 2 U/ml RNase inhibitor, 2.5 mM Stereo-seq-TSO and 1 x First-Strand buffer). After reverse transcription, tissue sections were washed twice with 0.1 3 SSC buffer and digested with Tissue Removal buffer (10 mM Tris-HCl, 25 mM EDTA, 100 mM NaCl, 0.5% SDS) at 37C for 30 minutes. cDNA-containing chips were then subjected to Exonuclease I (NEB, M0293L) treatment for 1 hour at 37°C and were finally washed once with 0.1x SSC buffer.

Amplification. The resulting cDNAs were amplified with KAPA HiFi Hotstart Ready Mix (Roche, KK2602) with 0.8 mM cDNA-PCR primer. PCR reactions were conducted as follows: incubation at 95°C for 5 minutes, 15 cycles at 98°C for 20 seconds, 58°C for 20 seconds, 72°C for 3 minutes and a final incubation at 72ºC for 5 minutes.

Library construction and sequencing. The concentrations of the resulting PCR products were quantified by Qubit dsDNA Assay Kit (Thermo, Q32854). A total of 20 ng of DNA were then fragmented with in-house Tn5 transposase at 55°C for 10 minutes, after which the reactions were stopped by the addition of 0.02% SDS and gently mixing at 37°C for 5 minutes after fragmentation. Fragmented products were amplified as described below: 25 ml of fragmentation product, 1 3 KAPA HiFi Hotstart Ready Mix and 0.3 mM Stereo-seq-Library-F primer, 0.3 mM Stereo-seq-Library-R primer in a total volume of 100 ml with the addition of nuclease-free H2O. The reaction was then run as: 1 cycle of 95°C 5 minutes, 13 cycles of 98°C 20 seconds, 58°C 20 seconds and 72°C 30 seconds, and 1 cycle of 72°C 5 minutes. PCR products were purified using the AMPure XP Beads (0.63 and 0.153), used for DNB generation and finally sequenced on MGI DNBSEQ-Tx sequencer with read length.

Stereo-seq raw data processing. Fastq files were generated using a MGI DNBSEQ-Tx sequencer. CID and MID are contained in the read 1 (CID: 1-25 bp, MID: 26-35 bp) while the read 2 consist of the cDNA sequences. CID sequences on the first reads were first mapped to the designed coordinates of the in situ captured chip achieved from the first round of sequencing, allowing 1 base mismatch to correct for sequencing and PCR errors. Reads with MID containing either N bases or more than 2 bases with quality score lower than 10 were filtered out. CID and MID associated with each read were appended to each read header. Retained reads were then aligned to the reference genome (mm10) using STAR (Dobin et al., 2013) and mapped reads with MAPQ > 10 were counted and annotated to their corresponding genes). UMI with the same CID and the same gene locus collapsed, allowing 1 mismatch to correct for sequencing and PCR errors. Finally, this information was used to generate a CID-containing expression profile matrix. The whole procedure was integrated into a publicly available pipeline SAW available at https://github.com/BGIResearch/SAW.

Electrophysiology

Male and female mice (wild-type, C57BL/6) 3 months of age were anesthetized with isoflurane using the bell jar method and rapidly decapitated. The brain was dissected in ice cold, oxygenated standard artificial cerebrospinal fluid (ACSF) containing, in mM: 126 NaCl, 3 KCl, 25 NaHCO3, 1 NaHPO4, 2 MgSO4, 2 CaCl2, 14 dextrose with an osmolarity of 313-317mOsm and a pH = 7.4 when oxygenated with carbogen (95% oxygen, 5% carbon dioxide). Coronal

slices (400µm) containing CA1 were prepared using a fresh tissue vibratome (Leica VT1000), allowed to recover in 34°C ACSF for 40min, and then brought to room temperature for 30min before beginning experiments. Individual slices were transferred to a holding chamber for a 30-minute pre-incubation with Aβ or gAβ dissolved in oxygenated ACSF. Pre-incubation with PBS was used as a control condition. Final concentrations of Aβ (2µM) and gAβ (2µM) dilutions were prepared fresh daily from 100 µM stock solutions. After the pre-incubation, slices were transferred to the recording chamber, perfused with ACSF and maintained at 34°C with an inline heater (Warner Instruments).

To record field-excitatory post-synaptic potentials (fEPSPs), a bipolar tungsten stimulating electrode (Microprobes for Life Science) and a recording electrode were placed in the CA1 stratum radiatum. The recording electrode was a glass pipette with a resistance of 4–8MΩ, filled with ACSF. For each recording, an input/output curve was collected using a series of stimulation intensities. The experiment was then conducted using a stimulation intensity that elicited approximately 30% of the maximal fEPSP response. Single baseline pulses were delivered every 20 seconds for 20 minutes to establish a baseline. To induce Long Term Potentiation (LTP) theta-burst stimulation (TBS) consisting of 3x10 bursts of 4 pulses at 100Hz delivered at 5Hz were used. After induction, fEPSPs were recorded every 20 seconds for 60 minutes. The magnitude of plasticity was quantified as the fEPSP slope between 20% to 80% of the peak amplitude using custom scripts in Igor Pro (Wavemetrics). Post-tetanic potentiation was measured in the first 5 minutes following TBS, while LTP magnitude was quantified by averaging fEPSP slopes in the last 5 minutes of the recordings. The fEPSP measurements are presented as the mean ± SEM as a percent change relative to the mean baseline slope.

Mice behavior studies

Spatial learning and memory were investigated with the Morris Water Maze (MWM) and Nest behavior test were performed after four weeks of inhibitor administration. Mice were subjected to the MWM hidden platform test as described previously[53]. Briefly, mice were trained for five consecutive days with four trials per mouse per day. On the last day, a probe trial was performed to assess the spatial memory of the mice. Traces of mice were recorded, and data were analyzed using HVS Image 2014. All animals were individually coded, and investigators were blinded to the mouse for the duration of behavioral testing. For Nesting behavior study, each cage is supplied with a 'Nestlet,' a 5 × 5 cm square of pressed cotton batting (Ancare, Cat# NES3600), for three days prior to measuring nesting capability. For assessment, mice were housed individually with normal bedding and given an intact, pre-weighed cotton nestlet (3.0 g; Ancare). After 24 h, images were taken for each nest. Nest quality was scored on a scale of 1 to 5, according to our previously published criteria[37], with 1 being largely untorn nestlets and 5 being near perfect nests.

Statistical analysis

The sample size was not predetermined using any statistical techniques. Except where noted specifically, neither humans nor animals were excluded from the analysis. All appropriate data were analyzed using StatView statistics software or GraphPad Prism 8. All hypothesis tests were performed as two-tailed tests. Specific statistical analysis methods are described in the related figure legends where results are presented. All data were expressed as the mean ± SD or ± SE. Values were considered statistically significant for P values <0.05.

References

1. Trujillo, M.N. & Galligan, J.J. Reconsidering the role of protein glycation in disease. *Nat Chem Biol* **19**, 922-927 (2023).
2. Münch, G., Thome, J., Foley, P., Schinzel, R. & Riederer, P. Advanced glycation endproducts in ageing and Alzheimer's disease. *Brain research reviews* **23**, 134-143 (1997).
3. Yan, S.D*., et al.* Non-enzymatically glycated tau in Alzheimer's disease induces neuronal oxidant stress resulting in cytokine gene expression and release of amyloid beta-peptide. *Nat Med* **1**, 693-699 (1995).
4. Li, X.H*., et al.* Glycation exacerbates the neuronal toxicity of β-amyloid. *Cell Death Dis* **4**, e673 (2013).
5. Valente, T., Gella, A., Fernàndez-Busquets, X., Unzeta, M. & Durany, N. Immunohistochemical analysis of human brain suggests pathological synergism of Alzheimer's disease and diabetes mellitus. *Neurobiol Dis* **37**, 67-76 (2010).
6. Sasaki, N*., et al.* Advanced glycation end products in Alzheimer's disease and other neurodegenerative diseases. *Am J Pathol* **153**, 1149-1155 (1998).
7. Smith, M.A*., et al.* Advanced Maillard reaction end products are associated with Alzheimer disease pathology. *Proc Natl Acad Sci U S A* **91**, 5710-5714 (1994).
8. Lüth, H.-J*., et al.* Age- and Stage-dependent Accumulation of Advanced Glycation End Products in Intracellular Deposits in Normal and Alzheimer's Disease Brains. *Cerebral Cortex* **15**, 211-220 (2004).
9. Yan, S.D*., et al.* RAGE and amyloid-β peptide neurotoxicity in Alzheimer's disease. *Nature* **382**, 685-691 (1996).
10. Schmidt, A.M., Du Yan, S., Yan, S.F. & Stern, D.M. The multiligand receptor RAGE as a progression factor amplifying immune and inflammatory responses. *The Journal of clinical investigation* **108**, 949-955 (2001).
11. Decout, A., Katz, J.D., Venkatraman, S. & Ablasser, A. The cGAS–STING pathway as a therapeutic target in inflammatory diseases. *Nature Reviews Immunology* **21**, 548-569 (2021).
12. Motwani, M., Pesiridis, S. & Fitzgerald, K.A. DNA sensing by the cGAS–STING pathway in health and disease. *Nature Reviews Genetics* **20**, 657-674 (2019).
13. Lin, M.-m., Liu, N., Qin, Z.-h. & Wang, Y. Mitochondrial-derived damage-associated molecular patterns amplify neuroinflammation in neurodegenerative diseases. *Acta Pharmacologica Sinica* **43**, 2439-2447 (2022).
14. Bai, J*., et al.* Mitochondrial stress-activated cGAS-STING pathway inhibits thermogenic program and contributes to overnutrition-induced obesity in mice. *Communications Biology* **3**, 257 (2020).
15. Riley, J.S. & Tait, S.W. Mitochondrial DNA in inflammation and immunity. *EMBO Rep* **21**, e49799 (2020).
16. Wang, X*., et al.* Driving axon regeneration by orchestrating neuronal and non-neuronal innate immune responses via the IFNγ-cGAS-STING axis. *Neuron* **111**, 236-255.e237 (2023).
17. Shoshan-Barmatz, V., Krelin, Y. & Shteinfer-Kuzmine, A. VDAC1 functions in Ca(2+) homeostasis and cell life and death in health and disease. *Cell Calcium* **69**, 81-100 (2018).
18. Cheng, E.H., Sheiko, T.V., Fisher, J.K., Craigen, W.J. & Korsmeyer, S.J. VDAC2 inhibits BAK activation and mitochondrial apoptosis. *Science* **301**, 513-517 (2003).
19. Kim, J*., et al.* VDAC oligomers form mitochondrial pores to release mtDNA fragments and promote lupus-like disease. *Science* **366**, 1531-1536 (2019).
20. McDonnell, M.A., Wang, D., Khan, S.M., Vander Heiden, M.G. & Kelekar, A. Caspase-9 is activated in a cytochrome c-independent manner early during TNFα-induced apoptosis in murine cells. *Cell Death & Differentiation* **10**, 1005-1015 (2003).
21. Emendato, A*., et al.* Glycation affects fibril formation of Aβ peptides. *J Biol Chem* **293**, 13100-13111 (2018).
22. Halim, A*., et al.* Site-specific characterization of threonine, serine, and tyrosine glycosylations of amyloid precursor protein/amyloid beta-peptides in human cerebrospinal fluid. *Proc Natl Acad Sci U S A* **108**, 11848-11853 (2011).
23. Szego, E.M*., et al.* Constitutively active STING causes neuroinflammation and degeneration of dopaminergic neurons in mice. *Elife* **11**(2022).
24. Jiang, S*., et al.* Mfn2 ablation causes an oxidative stress response and eventual neuronal death in the hippocampus and cortex. *Molecular Neurodegeneration* **13**, 5 (2018).

25. Berman, S.B., Pineda, F.J. & Hardwick, J.M. Mitochondrial fission and fusion dynamics: the long and short of it. *Cell Death & Differentiation* **15**, 1147-1152 (2008).
26. Lewis, T.L., Kwon, S.-K., Lee, A., Shaw, R. & Polleux, F. MFF-dependent mitochondrial fission regulates presynaptic release and axon branching by limiting axonal mitochondria size. *Nature Communications* **9**, 5008 (2018).
27. Takuma, K.*, et al.* RAGE-mediated signaling contributes to intraneuronal transport of amyloid-beta and neuronal dysfunction. *Proc Natl Acad Sci U S A* **106**, 20021-20026 (2009).
28. Haythorne, E.*, et al.* Altered glycolysis triggers impaired mitochondrial metabolism and mTORC1 activation in diabetic β-cells. *Nature Communications* **13**, 6754 (2022).
29. Gottlieb, E., Armour, S.M., Harris, M.H. & Thompson, C.B. Mitochondrial membrane potential regulates matrix configuration and cytochrome c release during apoptosis. *Cell Death Differ* **10**, 709-717 (2003).
30. McArthur, K.*, et al.* BAK/BAX macropores facilitate mitochondrial herniation and mtDNA efflux during apoptosis. *Science* **359**(2018).
31. Yu, C.-H.*, et al.* TDP-43 Triggers Mitochondrial DNA Release via mPTP to Activate cGAS/STING in ALS. *Cell* **183**, 636-649.e618 (2020).
32. Suzuki, K.*, et al.* Bax-inhibiting peptide attenuates bleomycin-induced lung injury in mice. *Biol Open* **6**, 1869-1875 (2017).
33. Wang, Y.*, et al.* Pathological convergence of APP and SNCA deficiency in hippocampal degeneration of young rats. *Cell Death Dis* **14**, 325 (2023).
34. Tamburrino, A.*, et al.* Cyclosporin promotes neurorestoration and cell replacement therapy in pre-clinical models of Parkinson's disease. *Acta Neuropathologica Communications* **3**, 84 (2015).
35. Xian, H.*, et al.* Oxidized DNA fragments exit mitochondria via mPTP- and VDAC-dependent channels to activate NLRP3 inflammasome and interferon signaling. *Immunity* **55**, 1370-1385.e1378 (2022).
36. Focusing on mitochondrial form and function. *Nature Cell Biology* **20**, 735-735 (2018).
37. Akhter, F.*, et al.* High Dietary Advanced Glycation End Products Impair Mitochondrial and Cognitive Function. *J Alzheimers Dis* **76**, 165-178 (2020).
38. Chen, A.*, et al.* Spatiotemporal transcriptomic atlas of mouse organogenesis using DNA nanoball-patterned arrays. *Cell* **185**, 1777-1792.e1721 (2022).
39. Drmanac, R.*, et al.* Human genome sequencing using unchained base reads on self-assembling DNA nanoarrays. *Science* **327**, 78-81 (2010).
40. Ng, J.*, et al.* Site-specific glycation of Aβ1-42 affects fibril formation and is neurotoxic. *J Biol Chem* **294**, 8806-8818 (2019).
41. Xie, X.*, et al.* Activation of innate immune cGAS-STING pathway contributes to Alzheimer's pathogenesis in 5×FAD mice. *Nat Aging* **3**, 202-212 (2023).
42. Gulen, M.F.*, et al.* cGAS–STING drives ageing-related inflammation and neurodegeneration. *Nature* **620**, 374-380 (2023).
43. Udeochu, J.C.*, et al.* Tau activation of microglial cGAS–IFN reduces MEF2C-mediated cognitive resilience. *Nature Neuroscience* **26**, 737-750 (2023).
44. Ablasser, A.*, et al.* Cell intrinsic immunity spreads to bystander cells via the intercellular transfer of cGAMP. *Nature* **503**, 530-534 (2013).
45. Luteijn, R.D.*, et al.* SLC19A1 transports immunoreactive cyclic dinucleotides. *Nature* **573**, 434-438 (2019).
46. Hansson Petersen, C.A.*, et al.* The amyloid beta-peptide is imported into mitochondria via the TOM import machinery and localized to mitochondrial cristae. *Proc Natl Acad Sci U S A* **105**, 13145-13150 (2008).
47. Verma, A.*, et al.* The role of the mitochondrial protein VDAC1 in inflammatory bowel disease: a potential therapeutic target. *Mol Ther* **30**, 726-744 (2022).
48. Wu, N.N.*, et al.* Site-specific ubiquitination of VDAC1 restricts its oligomerization and mitochondrial DNA release in liver fibrosis. *Exp Mol Med* **55**, 269-280 (2023).
49. Yan, S.F., Akhter, F., Sosunov, A.A. & Yan, S.S. Identification and Characterization of Amyloid-β Accumulation in Synaptic Mitochondria. *Methods Mol Biol* **1779**, 415-433 (2018).

50. Budd, S.L., Tenneti, L., Lishnak, T. & Lipton, S.A. Mitochondrial and extramitochondrial apoptotic signaling pathways in cerebrocortical neurons. *Proc Natl Acad Sci U S A* **97**, 6161-6166 (2000).
51. Du, H.*, et al.* Cyclophilin D deficiency attenuates mitochondrial and neuronal perturbation and ameliorates learning and memory in Alzheimer's disease. *Nat Med* **14**, 1097-1105 (2008).
52. Akhter, F., Chen, D., Akhter, A., Yan, S.F. & Yan, S.S. Age-dependent accumulation of dicarbonyls and advanced glycation endproducts (AGEs) associates with mitochondrial stress. *Free Radic Biol Med* **164**, 429-438 (2021).
53. Vorhees, C.V. & Williams, M.T. Morris water maze: procedures for assessing spatial and related forms of learning and memory. *Nat Protoc* **1**, 848-858 (2006).

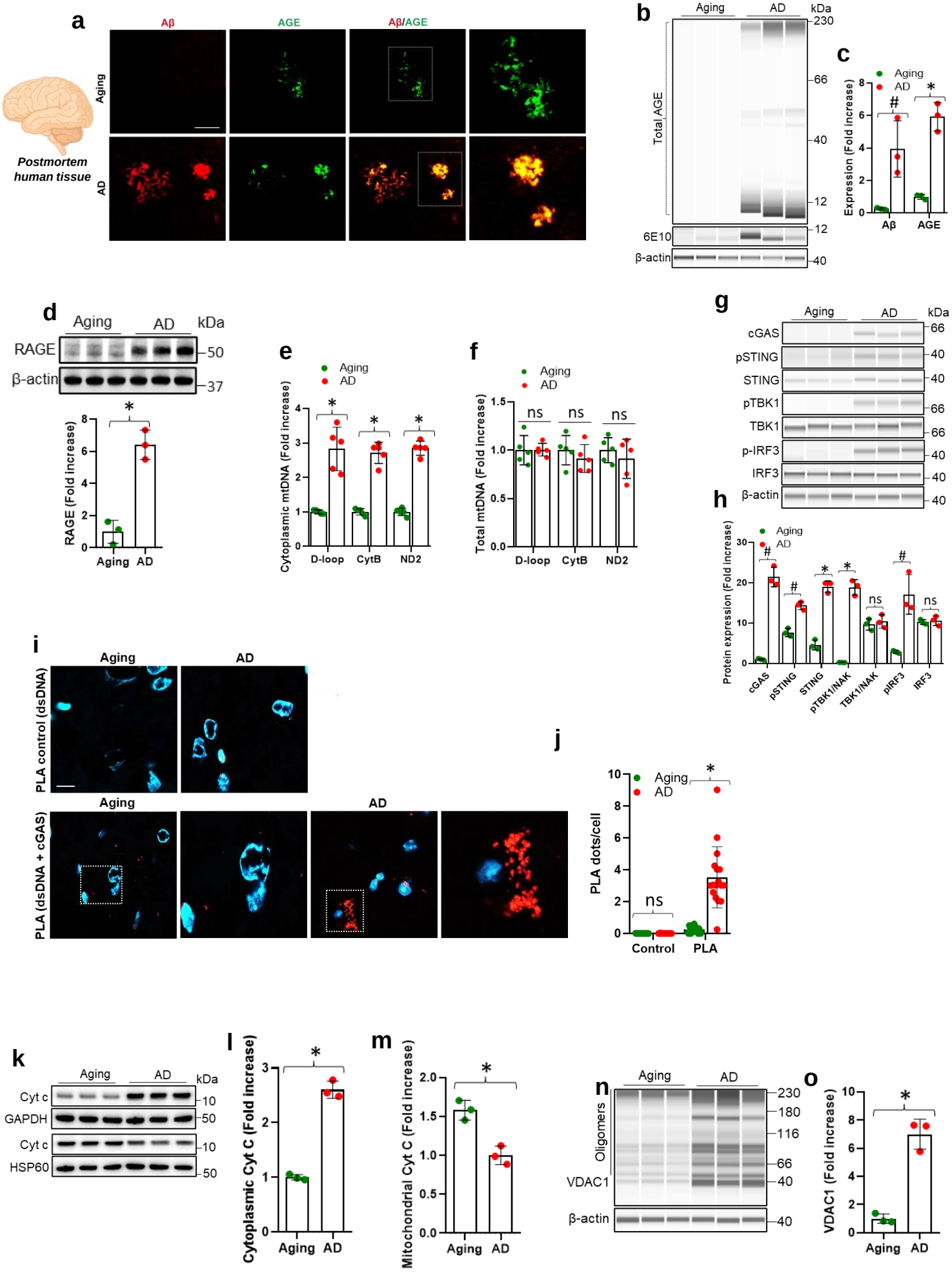
a
Aβ
AGE
Aβ/AGE
Aging
AD
Postmortem human tissue
b
Aging
AD
kDa
230
66
40
12
Total AGE
6E10
β-actin
c
Aging
AD
Expression (Fold increase)
Aβ
AGE
d
Aging
AD
kDa
RAGE
β-actin
50
37
RAGE (Fold increase)
e
Cytoplasmic mtDNA (Fold increase)
D-loop
CytB
ND2
f
Total mtDNA (Fold increase)
ns
g
cGAS
pSTING
STING
pTBK1
TBK1
p-IRF3
IRF3
h
Protein expression (Fold increase)
cGAS
pSTING
STING
pTBK1/NAK
TBK1/NAK
pIRF3
IRF3
i
PLA control (dsDNA)
PLA (dsDNA + cGAS)
j
PLA dots/cell
Control
PLA
k
Cyt c
GAPDH
HSP60
l
Cytoplasmic Cyt C (Fold increase)
m
Mitochondrial Cyt C (Fold increase)
n
Oligomers
VDAC1
β-actin
o
VDAC1 (Fold increase)

Fig. 1

Fig. 1. Increased Aβ glycation in human AD brain that is linked to mtDNA leakage and cGAS-STING activation. (**a**), Immunostaining of Aβ with total AGE in aging or AD human brain hippocampus. Scale bar, 50 μm. Representative images as shown were from the results of five samples in each group. (**b**), The cortical extracts from aging or AD were immunoprecipitated with AGE and re-probed with Aβ antibody (6E10). (**c**), Quantification of the expression of the total AGE density and Aβ relative to β-actin**.** Mean ± SD; n = 3; $^{\#}P < 0.05$, $^{*}P < 0.001$, two-tailed Student's *t*-test. (**d**), Immunoblotting analysis of the expression of RAGE and quantification relative to β-actin in the human samples. Age-matched normal samples were used as aging controls. Mean ± SD; n = 3; $^{*}P < 0.001$, two-tailed Student's *t*-test. (**e, f**), Quantification of cytoplasmic and total mitochondrial DNA (mtDNA) by qPCR in indicated AD samples. D-loop, CytB and ND2 are specific fragments or proteins encoded by the mitochondrial genome. Mean ± SD; n = 5; $^{*}P < 0.001$, or $^{ns}P > 0.05$, two-tailed Student's *t*-test. (**g, h**), Immunoblot analysis for the expression and quantification of the cGAS, p-STING, STING, p-TBK1, TBK1, and p-IRF3, IRF3 relative to β-actin. Mean ± SD; n = 3; $^{ns}P > 0.05$, $^{\#}P < 0.05$, $^{*}P < 0.001$, two tailed Student's *t*-test. (**i**), PLA with anti-dsDNA and anti-cGAS antibodies showing the association of cGAS protein with cytosolic or nuclear dsDNA in aging or AD human brain hippocampus. Anti-dsDNA antibody alone was used as the PLA control. Scale bar, 10 μm. (**j**), Quantification of PLA red dots per cell. Mean ± SD; n = 5, five sections of each brain sample were stained and counted; $^{*}P < 0.001$, or $^{ns}P > 0.05$ one-way analysis of variance (ANOVA) with Bonferroni's post hoc test. (**k-m**), Immunoblotting analysis of the expression and quantification of cytochrome c (Cyt c) relative to GAPDH or HSP60 in cytosolic and mitochondrial fraction respectively of the cortical aging or AD samples. Mean ± SD; n = 3; $^{*}P < 0.001$, two-tailed Student's *t*-test. (**n, o**), Immunoblotting analysis of the expression and quantification of VDAC1 relative to β-actin in indicated samples of aging or AD. Mean ± SD; n = 3; $^{*}P < 0.001$, two-tailed Student's *t*-test.

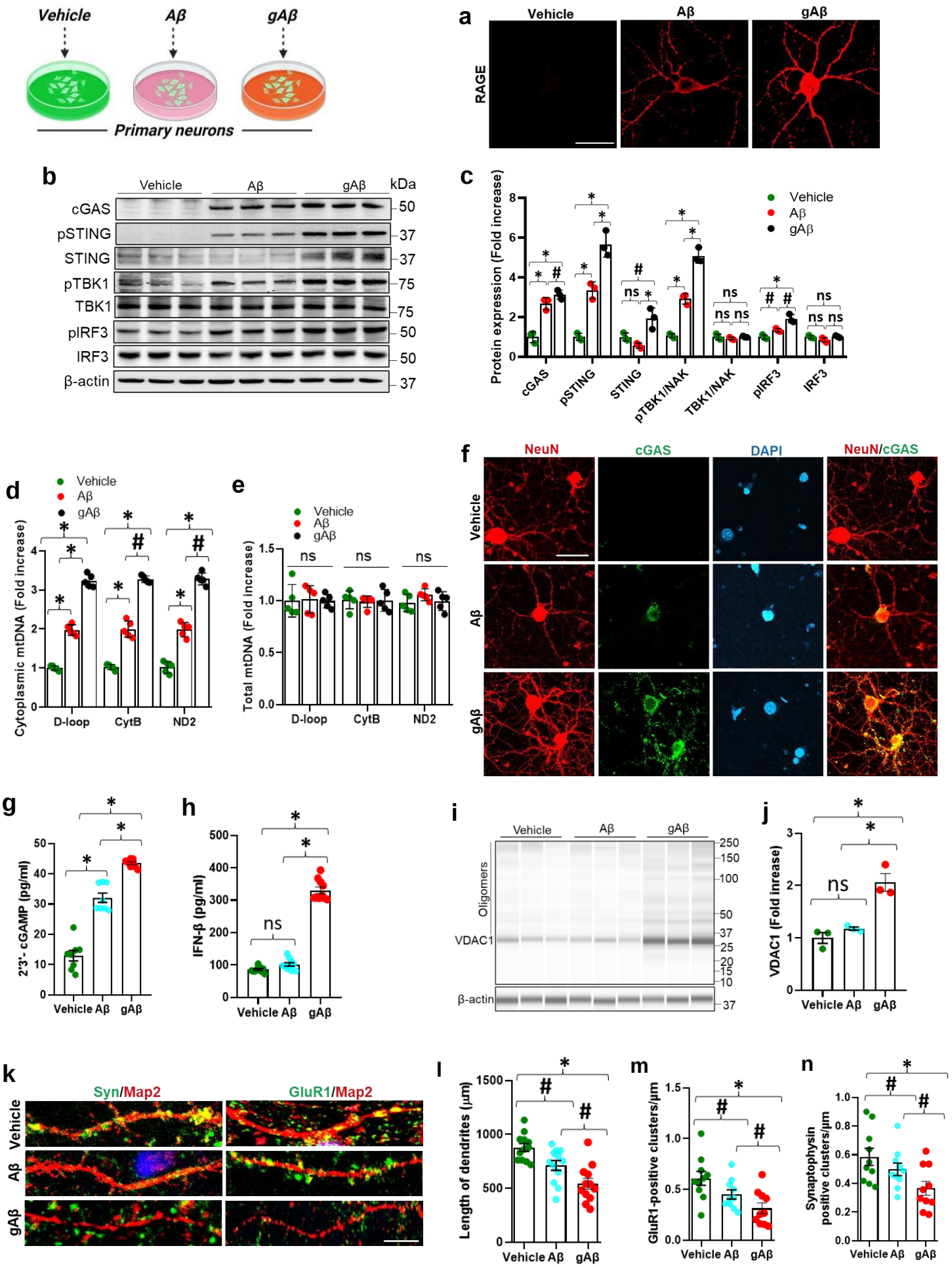
Vehicle
Aβ
gAβ
Primary neurons
a
RAGE
b
kDa
cGAS
pSTING
STING
pTBK1
TBK1
pIRF3
IRF3
β-actin
c
Protein expression (Fold increase)
cGAS
pSTING
STING
pTBK1/NAK
TBK1/NAK
pIRF3
IRF3
d
Cytoplasmic mtDNA (Fold increase)
D-loop
CytB
ND2
e
Total mtDNA (Fold increase)
f
NeuN
cGAS
DAPI
NeuN/cGAS
g
2'3'- cGAMP (pg/ml)
h
IFN-β (pg/ml)
i
Oligomers
VDAC1
β-actin
j
VDAC1 (Fold inrease)
k
Syn/Map2
GluR1/Map2
l
Length of dendrites (μm)
m
GluR1-positive clusters/μm
n
Synaptophysin positive clusters/μm

Fig. 2

Fig. 2. Aβ glycation exacerbates neuronal mitochondrial stress and neuroinflammation *in vitro*. (**a**) Immunostaining of RAGE in hippocampal neurons (DIV 10) treated with vehicle, Aβ or gAβ for 24 h. Scale bar, 50 μm. Representative images as shown were from the results of five samples in each group. (**b, c**), Immunoblot analysis for the expression and quantification of the expression of the cGAS, p-STING, STING, p-TBK1, TBK1, and p-IRF3, IRF3 relative to β-actin in the indicated hippocampal neuronal lysate. Mean ± SD; n = 3; $^{ns}P > 0.05$, $^{\#}P < 0.05$, $^{*}P < 0.01$, one-way ANOVA with Bonferroni's post hoc test. (**d, e**), Quantification of cytoplasmic and total mitochondrial DNA (mtDNA) by qPCR in indicated cultured neurons with vehicle, Aβ or gAβ treatment for 24 h. D-loop, CytB and ND2 are specific fragments or proteins encoded by the mitochondrial genome. Mean ± SD; n = 5; $^{*}P < 0.01$, $^{\#}P < 0.05$, or $^{ns}P > 0.05$, one-way ANOVA with Bonferroni's post hoc test. (**f**), Immunostaining of cGAS with NeuN in hippocampal neurons (DIV 8), treated with vehicle, Aβ or gAβ for 24 h. Scale bar, 50 μm. Representative images as shown were from the results of five samples in each group. (**g**), ELISA analysis of 2′ 3′ -cGAMP level in vehicle, Aβ or gAβ treated primary neurons with the indicated treatment conditions. Mean ± SD; n = 8, $^{ns}P>0.05$; $^{*}P < 0.001$; one-way ANOVA with Bonferroni's post hoc test. (**h**), ELISA analysis of IFN-β level in the supernatants of indicated primary neurons treated with vehicle, Aβ or gAβ. Mean ± SD; n = 10, $^{ns}P>0.05$; $^{*}P < 0.001$; one-way ANOVA with Bonferroni's post hoc test. (**i, j**), Immunoblotting analysis of the expression and quantification of VDAC1 relative to β-actin in indicated neurons (DIV 10) with the same treatment conditions. Mean ± SD; n = 3; $^{ns}P > 0.05$, $^{*}P < 0.001$, one-way ANOVA with Bonferroni's post hoc test. (**k**), Representative images show that gAβ decreased the density of synaptophysin-positive clusters near or on dendrites compared to Aβ or vehicle treated neurons (DIV 10) with the same treatment conditions. Neurons were immunostained with MAP2 and GluR1 as a post-synaptic marker and synaptophysin as presynaptic marker. (**l-n**), Quantification of synaptophysin-positive clusters per μm of dendrite length. Scale bar, 5 μm. Mean ± SD; n = 10; $^{\#}P < 0.05$, $^{*}P < 0.01$, one-way ANOVA with Bonferroni's post hoc test.

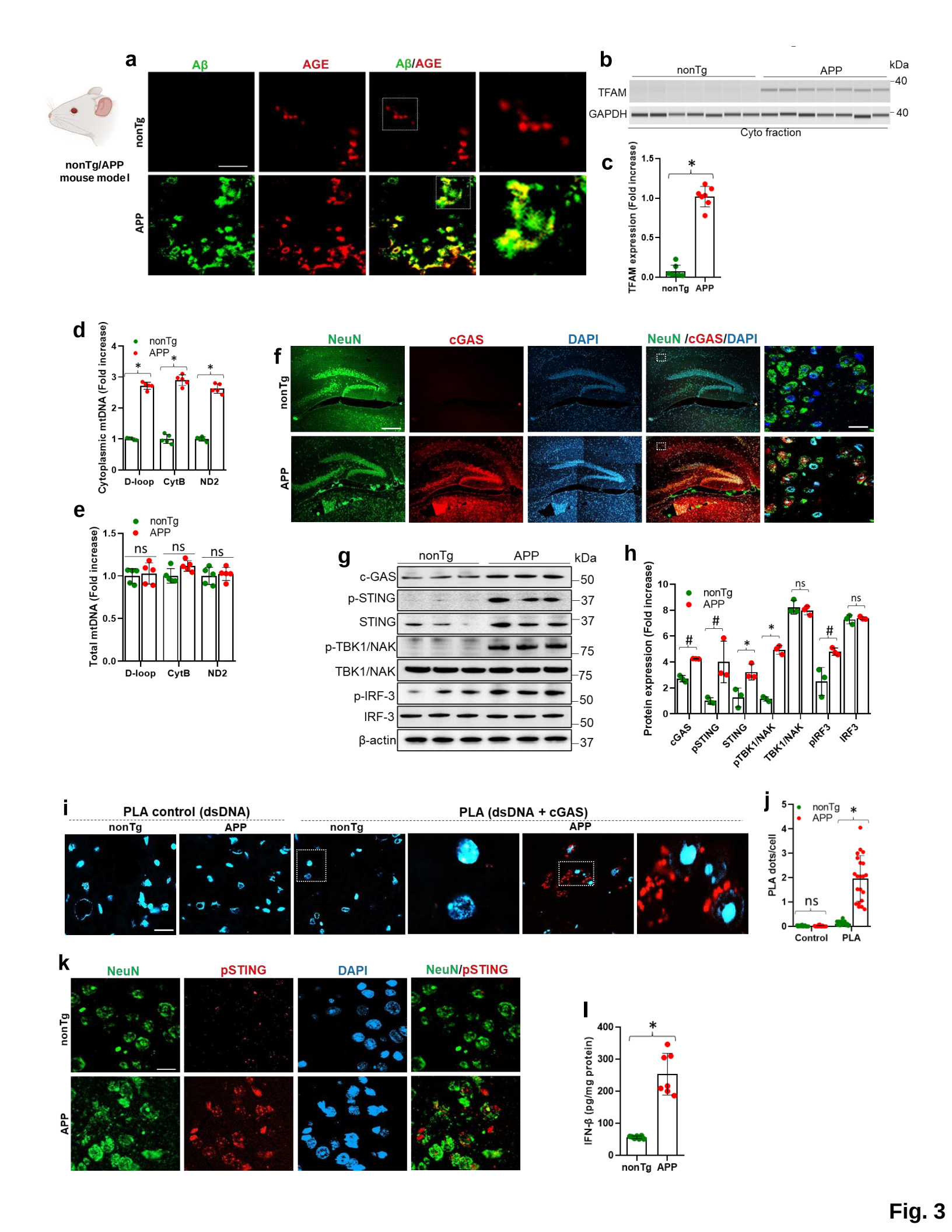
a
Aβ
AGE
Aβ/AGE
nonTg
APP
nonTg/APP mouse model
b
nonTg
APP
kDa
TFAM
GAPDH
40
40
Cyto fraction
c
TFAM expression (Fold increase)
nonTg
APP
d
nonTg
APP
Cytoplasmic mtDNA (Fold increase)
D-loop
CytB
ND2
e
nonTg
APP
Total mtDNA (Fold increase)
ns
D-loop
CytB
ND2
f
NeuN
cGAS
DAPI
NeuN /cGAS/DAPI
nonTg
APP
g
nonTg
APP
kDa
c-GAS
p-STING
STING
p-TBK1/NAK
TBK1/NAK
p-IRF-3
IRF-3
β-actin
50
37
37
75
75
50
50
37
h
nonTg
APP
Protein expression (Fold increase)
cGAS
pSTING
STING
pTBK1/NAK
TBK1/NAK
pIRF3
IRF3
ns
i
PLA control (dsDNA)
PLA (dsDNA + cGAS)
nonTg
APP
nonTg
APP
j
nonTg
APP
PLA dots/cell
ns
Control
PLA
k
NeuN
pSTING
DAPI
NeuN/pSTING
nonTg
APP
l
IFN-β (pg/mg protein)
nonTg
APP

Fig. 3

Fig. 3. Increased Aβ glycation in APP mice that induces mtDNA leakage and cGAS-STING activation. (a), Immunostaining of total AGE with Aβ in 8-month-old nonTg and APP. Scale bar, 100 μm. Representative images as shown were from the results of three mice in each group. (b, c), Immunoblotting analysis of the expression (b), and quantification (c) of TFAM in cytosolic fraction of the indicated mice relative to GAPDH. Mean ± SD; n = 7; *P < 0.001, two-tailed Student's t-test. (d, e), Quantification of cytoplasmic and total mitochondrial DNA (mtDNA) by quantitative PCR (qPCR) in brain cells of 8-month-old APP mice. Age-matched nonTg mice were used as controls. D-loop, CytB and ND2 are specific fragments or proteins encoded by the mitochondrial genome. Mean ± SD; n = 5; *P < 0.001, nsP > 0.05, two-tailed Student's t-test. (f), Immunostaining of cGAS with NeuN in Hippocampus of 8-month-old nonTg and APP mice. Scale bar, 200 μm (low power image) or 10 μm (high power image). Representative images as shown were from the results of 5 mice in each group. (g, h), Immunoblot analysis for the expression and quantification of the expression of the cGAS, p-STING, STING, p-TBK1, TBK1, and p-IRF3, IRF3 relative to β-actin. Mean ± SD; n = 3; nsP > 0.05, #P < 0.05, *P < 0.01, two tailed Student's t-test. (i), PLA with anti-dsDNA and anti-cGAS antibodies showing the association of cGAS protein with cytosolic or nuclear dsDNA in hippocampal tissues of 8-month-old APP mice. Anti-dsDNA antibody alone was used as the PLA control. Age-matched nonTg mice were used as control. Scale bar, 10 μm. (j) Quantification of PLA red dots per cell. Mean ± SD; n = 5, five sections of each brain sample were stained and counted; *P < 0.001, or nsP > 0.05 one-way analysis of variance (ANOVA) with Bonferroni's post hoc test. (k), Immunostaining of pSTING with NeuN in Hippocampus of 8-month-old nonTg and APP mice. Scale bar, 10 μm. Representative images as shown were from the results of 5 mice in each group. (l) ELISA analysis of IFN-β level in hippocampus of 8-month-old nonTg and APP mice. Mean ± SD; n = 7; *P < 0.001, two-tailed Student's t-test.

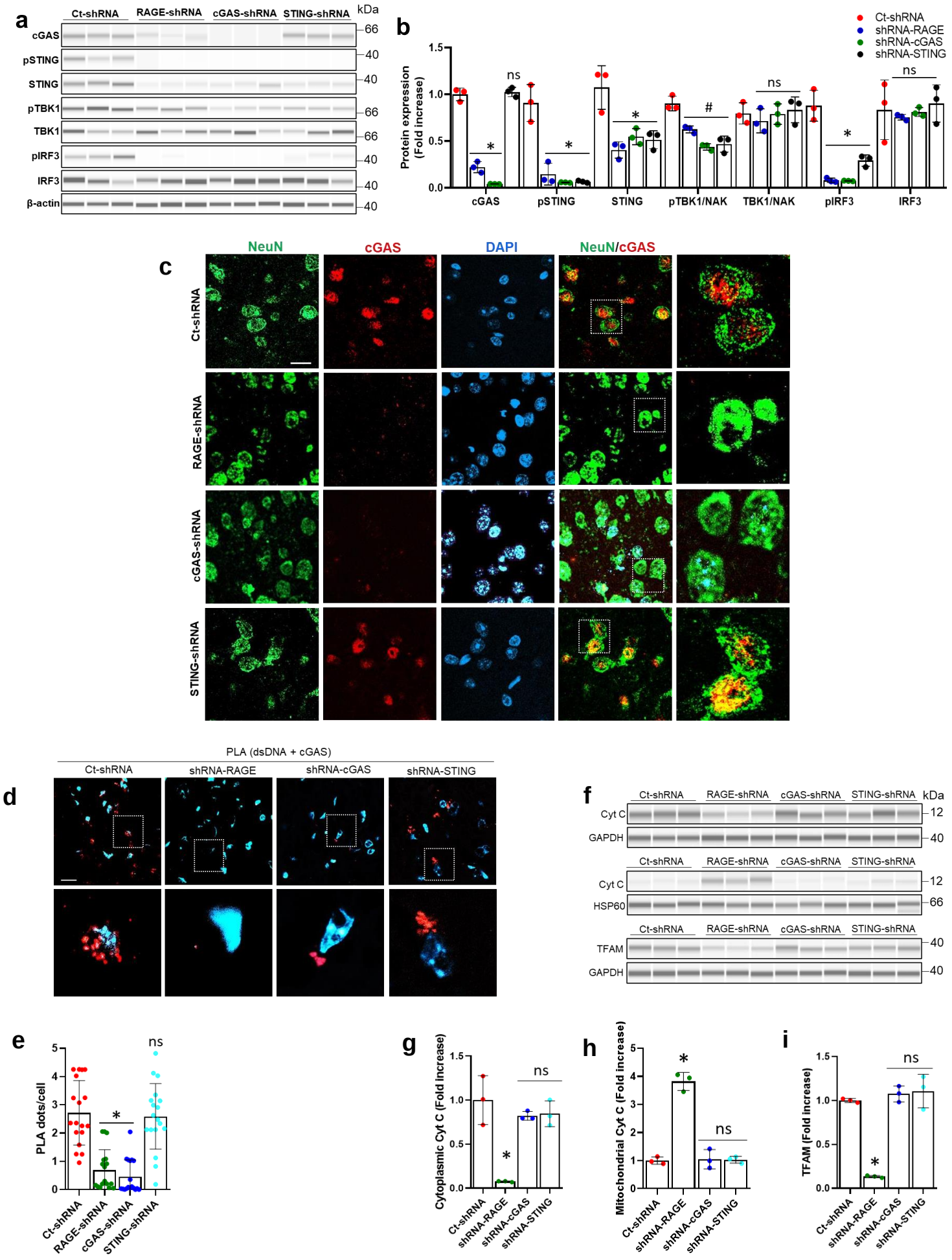
a
Ct-shRNA
RAGE-shRNA
cGAS-shRNA
STING-shRNA
kDa
cGAS
pSTING
STING
pTBK1
TBK1
pIRF3
IRF3
β-actin
66
40
b
Ct-shRNA
shRNA-RAGE
shRNA-cGAS
shRNA-STING
Protein expression (Fold increase)
ns
*
#
cGAS
pSTING
STING
pTBK1/NAK
TBK1/NAK
pIRF3
IRF3
c
NeuN
cGAS
DAPI
NeuN/cGAS
Ct-shRNA
RAGE-shRNA
cGAS-shRNA
STING-shRNA
d
PLA (dsDNA + cGAS)
Ct-shRNA
shRNA-RAGE
shRNA-cGAS
shRNA-STING
f
Cyt C
GAPDH
HSP60
TFAM
e
PLA dots/cell
g
Cytoplasmic Cyt C (Fold increase)
h
Mitochondrial Cyt C (Fold increase)
i
TFAM (Fold increase)

Fig. 4

Fig. 4. Knockdown of RAGE, cGAS, or STING attenuates mitochondrial dysfunction, mtDNA and cytochrome c release. (a) Immunoblotting analysis of the expression of the cGAS, p-STING, STING, p-TBK1, TBK1, and p-IRF3, IRF3 in the indicated samples; n = 3. (b), Quantification of the expression of the cGAS, p-STING, STING, p-TBK1, TBK1, and p-IRF3, IRF3 relative to β-actin. Mean ± SD; n = 3; nsP > 0.05, #P < 0.05, *P < 0.001, one-way analysis of variance (ANOVA) with Bonferroni's post hoc test. (c), Immunostaining of cGAS with NeuN in the hippocampal CA1 region of indicated mice. Scale bar, 10 μm. Representative images as shown were from the results of five samples in each group. (d), PLA with anti-dsDNA and anti-cGAS antibodies showing the association of cGAS protein with cytosolic or nuclear dsDNA in hippocampal CA1 region of the indicated mice. Scale bar, 10 μm. (e) Quantification of PLA red dots per cell. Mean ± SD; n = 5, five sections of each brain sample were stained and counted; nsP > 0.05, *P < 0.001, one-way analysis of variance (ANOVA) with Bonferroni's post hoc test. (f), Immunoblotting analysis of the expression of the cytochrome c (Cyt c) in the indicated samples cytosolic and mitochondrial fraction and TFAM in the cytosol; n = 3. (g, h), Quantification of the expression of the CytC relative to GAPDH or HSP60 in cytosolic and mitochondrial fraction respectively. Mean ± SD; n = 3; nsP > 0.05, *P < 0.001, one-way analysis of variance (ANOVA) with Bonferroni's post hoc test. (i), Quantification of the TFAM relative to GAPDH in cytosolic fraction. Mean ± SD; n = 3; nsP > 0.05, *P < 0.001, one-way analysis of variance (ANOVA) with Bonferroni's post hoc test.

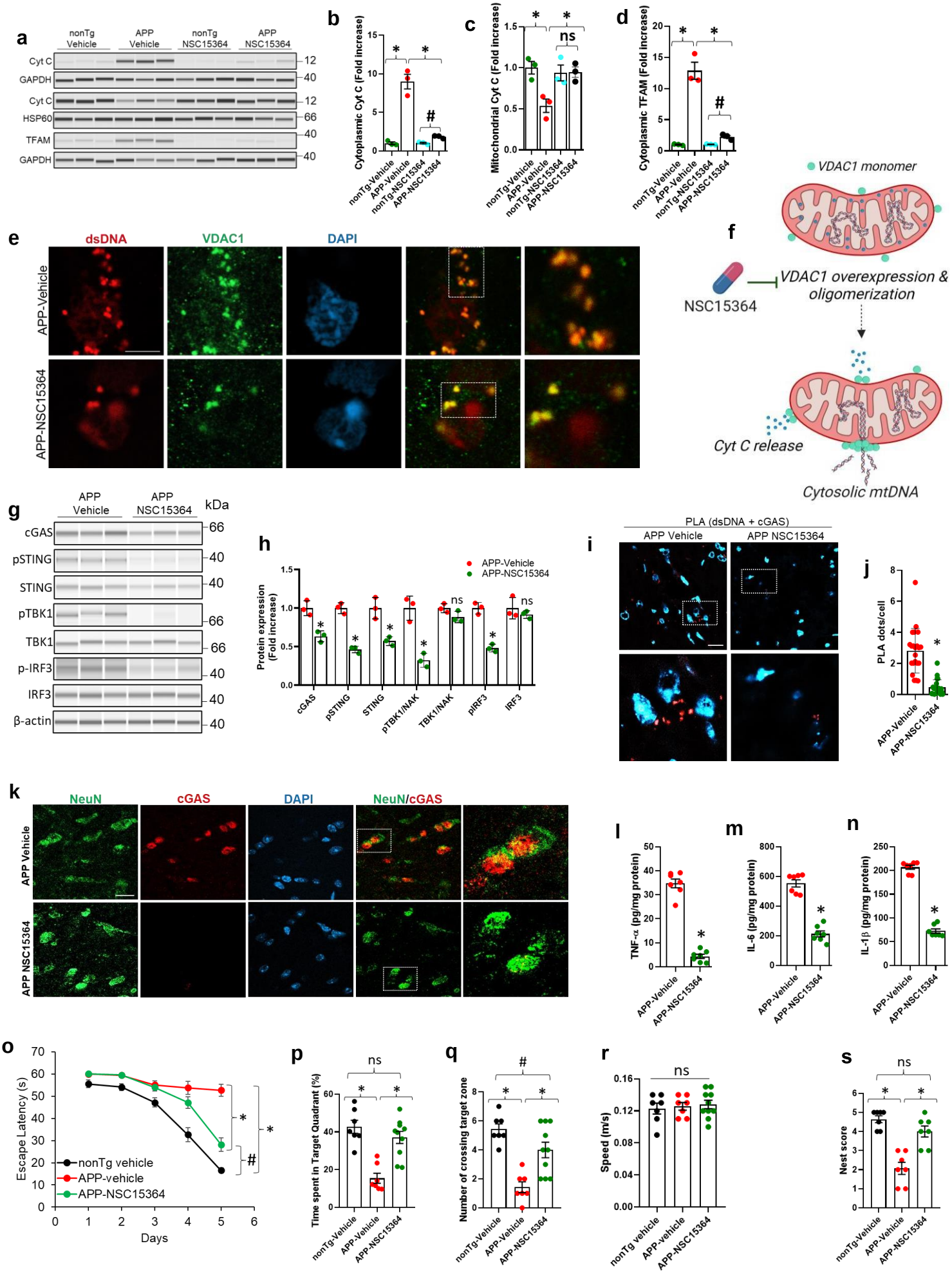
a
nonTg Vehicle
APP Vehicle
nonTg NSC15364
APP NSC15364
Cyt C
GAPDH
Cyt C
HSP60
TFAM
GAPDH
b
Cytoplasmic Cyt C (Fold increase)
c
Mitochondrial Cyt C (Fold increase)
ns
d
Cytoplasmic TFAM (Fold increase)
nonTg-Vehicle
APP-Vehicle
nonTg-NSC15364
APP-NSC15364
e
dsDNA
VDAC1
DAPI
APP-Vehicle
APP-NSC15364
f
VDAC1 monomer
NSC15364
VDAC1 overexpression & oligomerization
Cyt C release
Cytosolic mtDNA
g
APP Vehicle
APP NSC15364
kDa
cGAS
pSTING
STING
pTBK1
TBK1
p-IRF3
IRF3
β-actin
h
APP-Vehicle
APP-NSC15364
Protein expression (Fold increase)
cGAS
pSTING
STING
pTBK1/NAK
TBK1/NAK
pIRF3
IRF3
i
PLA (dsDNA + cGAS)
APP Vehicle
APP NSC15364
j
PLA dots/cell
APP-Vehicle
APP-NSC15364
k
NeuN
cGAS
DAPI
NeuN/cGAS
APP Vehicle
APP NSC15364
l
TNF-α (pg/mg protein)
m
IL-6 (pg/mg protein)
n
IL-1β (pg/mg protein)
o
Escape Latency (s)
Days
nonTg vehicle
APP-vehicle
APP-NSC15364
p
Time spent in Target Quadrant (%)
q
Number of crossing target zone
r
Speed (m/s)
s
Nest score

Fig. 5

Fig. 5. Inhibition of VDAC1 restrains mtDNA leakage, cytochrome c release, cGAS-STING signaling and neuroinflammation in APP mice. (a) Immunoblotting analysis of the expression of the cytochrome c (Cyt c) in the vehicle or NSC15364 administered APP hippocampal cytosolic and mitochondrial fraction and TFAM in cytosolic fraction of indicated samples. n = 3. (b, c), Quantification of the expression of the Cyt c relative to GAPDH or HSP60 in cytosolic and mitochondrial fraction respectively. Mean ± SD; n = 3; nsP > 0.05, #P < 0.05, *P < 0.001, one-way ANOVA with Bonferroni's post hoc test. (d), Quantification of the TFAM relative to GAPDH in cytosolic fraction. Mean ± SD; n = 3; #P < 0.05, *P < 0.001, one-way ANOVA with Bonferroni's post hoc test. (e), Immunostaining of dsDNA with VDAC1 in the hippocampal region of indicated mice. Scale bar, 10 μm. Representative images as shown were from the results of five samples in each group. (f), Schematic representation of the role of NSC15364 on VDAC1 oligomerization and subsequent protection against Cyt c and mtDNA release. (g), Immunoblotting analysis of the expression of the cGAS, p-STING, STING, p-TBK1, TBK1, and p-IRF3, IRF3 in the indicated mice hippocampal lysates; n = 3. (h), Quantification of the expression of the cGAS, p-STING, STING, p-TBK1, TBK1, and p-IRF3, IRF3 relative to β-actin. Mean ± SD; n = 3; nsP > 0.05, *P < 0.001, one-way ANOVA with Bonferroni's post hoc test. (i), PLA with anti-dsDNA and anti-cGAS antibodies showing the association of cGAS protein with cytosolic or nuclear dsDNA in hippocampal region of the indicated mice. Scale bar, 10 μm. (j), Quantification of PLA red dots per cell. Mean ± SD; n = 5, five sections of each brain sample were stained and counted; *P < 0.001, one-way ANOVA with Bonferroni's post hoc test. (k), Immunostaining of cGAS with NeuN in the hippocampal region of indicated mice. Scale bar, 10 μm. Representative images as shown were from the results of five samples in each group. (l-n). ELISA for TNF-α (l), IL-6 (m), and IL-1β (n) in indicated mice hippocampal protein. Mean ± SD; n = 7; *P < 0.001, one-way ANOVA with Bonferroni's post hoc test. (o-r), Escape latency during MWM hidden platform task in indicated mice (o), time spent in the quadrant with the hidden platform (p), mean number of crossings of the target during the probe test (q). Average swim speed of nonTg (vehicle-treated) and APP (NSC15364-treated) mice Morris Water Maze behavior task of mice (r). Mean ± SD; n = 7-10; nsP > 0.05, #P < 0.05, *P < 0.001, one-way ANOVA with Bonferroni's post hoc test. (s) Nest score based on nest building behavior. Nesting deficits indicated by incomplete nests and low nest score. Nesting ability indicated by complete nests, high nest score. Mean ± SD; n = 7; nsP > 0.05, *P < 0.001, one-way ANOVA with Bonferroni's post hoc test.

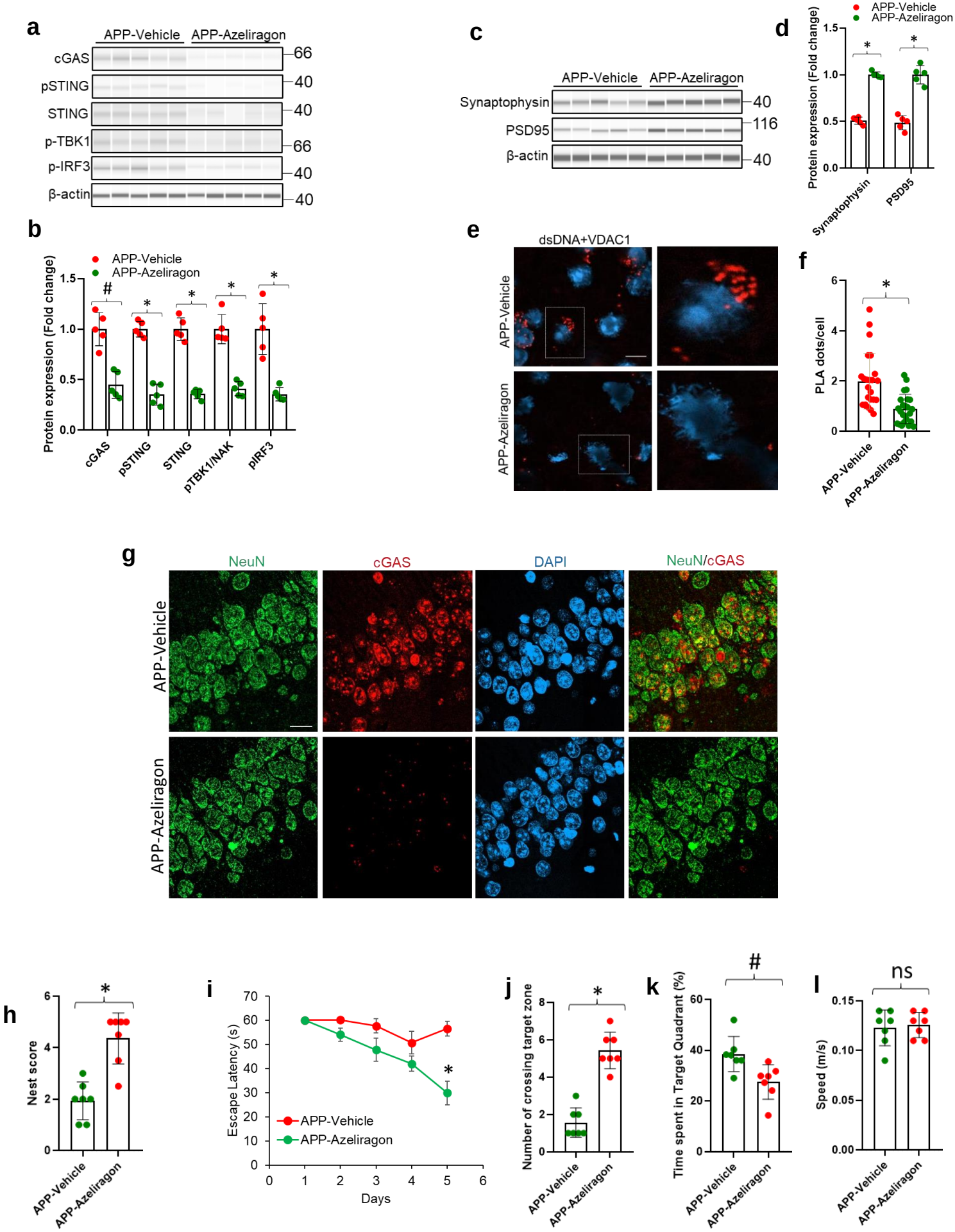
a
APP-Vehicle
APP-Azeliragon
cGAS
pSTING
STING
p-TBK1
p-IRF3
β-actin
66
40
40
66
40
40
b
APP-Vehicle
APP-Azeliragon
Protein expression (Fold change)
cGAS
pSTING
STING
pTBK1/NAK
pIRF3
c
APP-Vehicle
APP-Azeliragon
Synaptophysin
PSD95
β-actin
40
116
40
d
APP-Vehicle
APP-Azeliragon
Protein expression (Fold change)
Synaptophysin
PSD95
e
dsDNA+VDAC1
APP-Vehicle
APP-Azeliragon
f
PLA dots/cell
APP-Vehicle
APP-Azeliragon
g
NeuN
cGAS
DAPI
NeuN/cGAS
APP-Vehicle
APP-Azeliragon
h
Nest score
APP-Vehicle
APP-Azeliragon
i
Escape Latency (s)
Days
APP-Vehicle
APP-Azeliragon
j
Number of crossing target zone
APP-Vehicle
APP-Azeliragon
k
Time spent in Target Quadrant (%)
APP-Vehicle
APP-Azeliragon
l
Speed (m/s)
ns
APP-Vehicle
APP-Azeliragon

Fig. 6

Fig. 6. RAGE inhibition rescues cGAS-STING activation, neurodegeneration, and memory impairment in APP mice. (a) Immunoblotting analysis of the expression of the cGAS, p-STING, STING, p-TBK1, and p-IRF3, in six-week vehicle or Azeliragon treated APP mice (8-month-old); n = 5. (b), Quantification of the expressions of cGAS, p-STING, STING, p-TBK1, and p-IRF3 relative to β-actin. Mean ± SD; n = 5; #P < 0.05, *P < 0.001, one-way ANOVA with Bonferroni's post hoc test. (c), Immunoblotting analysis of the expression of pre-synaptic marker protein synaptophysin and postsynaptic density protein 95 (PSD95) in cortical tissues (including hippocampus) in n = 5. (d), Quantification of protein levels of Synaptophysin or PSD95 relative to β-actin. Mean ± SD; n = 5; *P < 0.001, one-way ANOVA with Bonferroni's post hoc test. (e), PLA with anti-dsDNA and anti-VDAC1 antibodies showing the association of VDAC1 protein with cytosolic or nuclear dsDNA in hippocampal CA1 region of the indicated mice. Scale bar, 10 μm. (f) Quantification of PLA red dots per cell. Mean ± SD; n = 5, five sections of each brain sample were stained and counted; *P < 0.001, one-way analysis of variance (ANOVA) with Bonferroni's post hoc test. (g), Immunostaining of cGAS with NeuN in Hippocampus of indicated mice. Scale bar, 10 μm. Representative images as shown were from the results of 5 mice in each group. (h), Nest score based on nest building behavior. Nesting deficits indicated by incomplete nests and low nest score. Nesting ability indicated by complete nests, high nest score. Mean ± SD; n = 7; *P < 0.01, one-way ANOVA with Bonferroni's post hoc test. (i-l), Escape latency during MWM hidden platform task in indicated mice (i), mean number of crossings of the target during the probe test (j), time spent in the quadrant with the hidden platform (k), and average swim speed (l) of mice in MWM Mean ± SD; n = 7-10; nsP > 0.05, #P < 0.05, *P < 0.01, one-way ANOVA with Bonferroni's post hoc test.